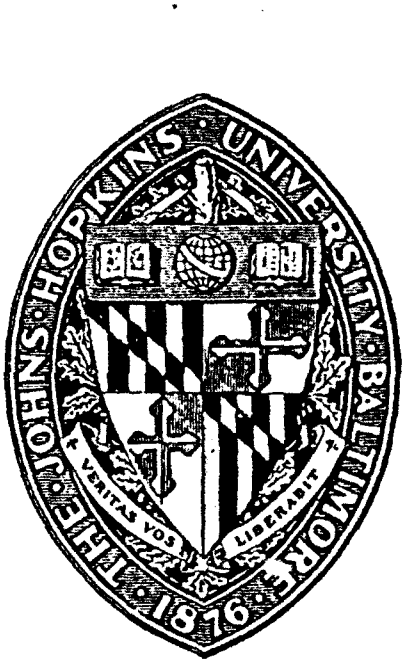

Effect of Microstructure on Passive Film Formation and Breakdown on Al Alloys

Grant No. N00014-89-J-1180

FINAL REPORT

By:

J. Kruger, J. W. Wagner, R. S. Lillard and C. C. Streinz
Materials Science and Engineering
The Johns Hopkins University
Baltimore, Maryland 21218

P. J. Moran
Mechanical Engineering
United States Naval Academy
Annapolis, Maryland 21402

Submitted to:

Dr. A. John Sedriks
Materials Division (Code 1131)
Office of Naval Research
Arlington, Virginia 22217

Effect of Microstructure on Passive Film Formation and Breakdown on Al Alloys

Grant No. N00014-89-J-1180

FINAL REPORT

By:

J. Kruger, J. W. Wagner, R. S. Lillard and C. C. Streinz
Materials Science and Engineering
The Johns Hopkins University
Baltimore, Maryland 21218

P. J. Moran
Mechanical Engineering
United States Naval Academy
Annapolis, Maryland 21402

Submitted to:

Dr. A. John Sedriks
Materials Division (Code 1131)
Office of Naval Research
Arlington, Virginia 22217

REPORT DOCUMENTATION PAGE

Form Approved
OMB No. 0704-0188

1. AGENCY USE ONLY (Leave blank)	2. REPORT DATE	3. REPORT TYPE AND DATES COVERED
	5/31/93	FINAL - 12/15/88-12/14/92

4. TITLE AND SUBTITLE

Effect of Microstructure on Passive Film Formation and Breakdown on Al Alloys

5. FUNDING NUMBERS

Grant No. N00014-89-J-1180
Modification No. P00003
R&T Project pasp001---05
S.O. Code: 1131M
Disbursing Code: N00179
AGO Code: N66002
CAGE Code: 5L406

6. AUTHOR(S)

J. Kruger, J. W. Wagner, R. S. Lillard, C. C. Streinz, and P. J. Moran

7. PERFORMING ORGANIZATION NAME(S) AND ADDRESS(ES)

The Johns Hopkins University
102 Maryland Hall
Baltimore, Maryland 21218

8. PERFORMING ORGANIZATION REPORT NUMBER

9. SPONSORING/MONITORING AGENCY NAME(S) AND ADDRESS(ES)

Office of Naval Research
800 North Quincy Street
Arlington, Virginia 22217 5000

10. SPONSORING/MONITORING AGENCY REPORT NUMBER

G.42.5032

11. SUPPLEMENTARY NOTES

12a. DISTRIBUTION/AVAILABILITY STATEMENT

Unlimited

12b. DISTRIBUTION CODE

13. ABSTRACT (Maximum 200 words)

Two *in situ* techniques, dynamic imaging microellipsometry (DIM) and local impedance spectroscopy (LEIS), were developed and applied to a study of the effect of microstructure on passive film formation and breakdown on Al-Ta alloys. DIM acquires ellipsometric data (thickness and optical constants of the films on surfaces) at a spatial resolution of *ca.* 20 μm using a radiometric full-field imaging approach. LEIS is an electrochemical impedance technique that generates local a.c. impedance data by measuring a.c. solution current densities very near the microstructural features of an electrode surface. The DIM technique was used to look at passive film formation at (*a*) the Al_3Ta precipitate, (*b*) the dealloyed zone adjacent to the precipitate and (*c*) the solid solution phase that is present in Al-Ta alloys. The DIM technique observed different film thicknesses and optical constants for the films that form on these phases at potentials in the passive regions. The LEIS technique was used to study the precipitate and the region surrounding it under conditions where passive film breakdown occurs. Using these techniques, insight was obtained into the passive film formation and breakdown processes that control localized corrosion.

14. SUBJECT TERMS

Al alloys, passive films, breakdown, microstructure, dynamic imaging microellipsometry, local electrochemical impedance spectroscopy

15. NUMBER OF PAGES

16. PRICE CODE

17. SECURITY CLASSIFICATION OF REPORT	18. SECURITY CLASSIFICATION OF THIS PAGE	19. SECURITY CLASSIFICATION OF ABSTRACT	20. LIMITATION OF ABSTRACT
Unclassified	Unclassified	Unclassified	

EFFECT OF MICROSTRUCTURE ON PASSIVE FILM FORMATION AND BREAKDOWN ON Al ALLOYS

This final report consists of a summary that describes the research carried out during the course of this study and three published papers giving the results of some of the research. Three more papers are being prepared for publication.

SUMMARY

1. DIM Studies

This research on the use of Dynamic Imaging Microellipsometry (DIM) to demonstrate the usefulness of the DIM technique for *in situ* examination of passive film growth on materials with microstructural heterogeneities. The focus of this study was the passive film formation on solid solution Al-Ta alloys and Al-Ta alloys containing Al_3Ta precipitates. Solid solution Al-Ta alloys possess dramatically improved resistance to pitting corrosion compared to pure aluminum. Passive film formation was monitored for alloyed compositions of pure Al, Al-8at%Ta, Al-25at%Ta and pure Ta at applied potentials of 0.0, 1.0, 2.0, and 5.0 V SCE. It was observed that increasing the concentration of tantalum in the solid solution alloys resulted in the formation of thinner passive films at all applied potentials. On pure Al and Al-8at%Ta, precipitation of an $Al(OH)_3$ type film results in a linearly increasing film thickness with time. The relationship of the film thickness measurements to the enhanced pitting resistance is discussed.

Al-Ta alloys are not thermodynamically stable in solid solution and when heat treated form Al_3Ta precipitates that act as sites for pit initiation and propagation. DIM was utilized to compare and contrast the thickness and refractive indices of the oxide film that forms on the precipitate with the film that forms on the matrix in order to examine their role in breakdown. Film formation was monitored for an Al-1.5at%Ta alloy, containing Al_3Ta precipitates on the order of 10-100 μm in diameter, at applied potentials of 0.0, 1.0, 2.0, and 5.0 V SCE. At 0.0 V SCE the passive film on the precipitate was observed to be thicker than that on the Al matrix. The film thicknesses at 1.0 V SCE were observed to be approximately equal, and at higher potentials (2.0 and 5.0 V SCE), the matrix was observed to form a thicker film than the precipitate. These results suggest that the interface between the two films is highly flawed, especially at potentials where there is a difference in the thickness between the two films. SEM observations demonstrate that the precipitate-matrix interface is susceptible to localized attack. It is proposed that pit initiation occurs at both the interface of the Al_3Ta and in the dealloyed region around the periphery of the precipitate. Both regions are demonstrated to be susceptible to initiation.

2. EIS and LEIS Studies

An investigation of passivity of single phase Al-Ta alloys and the contribution of the second phase, Al_3Ta, to breakdown is presented. In 0.1M NaCl buffered to Ph 7 with boric acid and sodium borate, the passive current density of pure aluminum was found to be approximately 0.3 microamps/cm^2, the passive current densities of Al4at%Ta, Al8at%Ta were found to be 2.5 and 2.4 microamps/cm^2 respectively, while the pitting potentials of these alloys were approximately 500 mV greater than that of pure aluminum. Traditional

Electrochemical Impedance Spectroscopy (EIS) measurement in 0.5M boric acid 0.05M sodium borate solution found the impedance values of the Al-4Ta and Al-8Ta were found to be 5.6×10^4 and 3.1×10^4 ohm cm^2 respectively while that of pure aluminum was found to be about 1.2×10^5 ohm cm^2. In addition, the thickness of the oxide film on the alloys to be less than that of pure aluminum in all solutions examined. Similar results were obtained for chloride containing solutions. These results indicate that there is no correlation between passive current density and the breakdown potential; that is the passive current density and the breakdown potential are two unrelated phenomena.

A technique, referred to as Local Electrochemical Impedance Spectroscopy (LEIS), for mapping the ac impedance distribution as a function of frequency for an electrode surface was developed. In this technique, as in traditional ac impedance methods, a sinusoidal voltage perturbation between the working and reference electrode is maintained by driving an ac current between the working and a distant counter electrode with a potentiostat. Local ac impedances are derived from the ratio of the applied ac voltage and the local ac solution current density. This local ac current density is obtained rom potential difference measurements near the electrode surface using a probe consisting of two microelectrodes. By measuring the ac potential difference between the microelectrodes, and knowledge of both the separation distance between the microelectrodes and the solution conductivity, the local ac solution current density is derived.

The accuracy of the local ac impedance data generated with this technique was established by investigating two systems. The first was a 99.999% aluminum sample. To create as homogenous a surface as possible, the electrode was polished and examined in a boric acid/sodium borate buffer solution (pH = 7.2) at a potential approximately 50 milli-volts anodic to E_{corr}. As expected, the local ac impedance measurements of this electrode, generated with the system LEIS system, agreed with the traditional ac impedance measurements for this electrode; further this agreement was found to be within 5%.

The results of LEIS experiments on a heat treated Al1.5at%Ta alloy which contained Al_3Ta precipitates, revealed that the capacitance of the film over the precipitate is higher than the capacitance of the film over the aluminum portion of this electrode. This indicates that thickness of the film over the precipitate is thinner than the film over aluminum. This interface, between the oxide over the Al_3Ta precipitates and the oxide over the aluminum matrix, is perceived as being incoherent and is interpreted here as a "residual flaw," as described by the crack/heal mechanism proposed by Wood et al.

Reprinted from JOURNAL OF THE ELECTROCHEMICAL SOCIETY
Vol. 139, No. 3, March 1992
Printed in U.S.A.

Analysis of Passive Film Growth by Dynamic Imaging Microellipsometry

C. C. Streinz,* J. W. Wagner, and J. Kruger**

Department of Materials Science and Engineering, The Johns Hopkins University, Baltimore, Maryland 21218

P. J. Moran**

Department of Mechanical Engineering, United States Naval Academy, Annapolis, Maryland 21402

ABSTRACT

Dynamic imaging microellipsometry (DIM) is a full field, radiometric approach to ellipsometry that provides high spatial resolution and accuracy. This paper reports on the latest DIM system and demonstrates the usefulness of the DIM technique for *in situ* examination of passive film growth on materials with microstructural inhomogeneities. In particular DIM has been utilized to examine passive film growth on a polycrystalline iron sample and an aluminum tantalum alloy that contained intermetallic precipitates. Grain orientation has been observed to affect the growth rate and final thickness of the film on iron. Ellipsometric identification of intermetallic precipitates (approximately 20 μm in diameter) is reported. The precipitates are observed to form a thinner passive film than the matrix. The incompatibility between the film over the precipitate and that over the matrix may degrade the localized corrosion behavior of these alloys.

Ellipsometry is an optical technique that enables the thickness and complex refractive index of thin films on metal surfaces to be measured *in situ* (1). Since many corrosion and electrochemical processes involve film formation and breakdown, ellipsometry has proven to be a valuable research tool for studying corrosion (2). Traditional ellipsometry, however, is by nature a surface averaging technique and is limited for studying localized corrosion processes such as the effects of microstructure on passive film growth and breakdown.

Several investigators (3-6) have attempted to overcome this limitation by scanning single-point ellipsometric measurements over a surface of interest. Sugimoto *et al.* (4, 5), examined passive films on duplex stainless steels and reported a spatial resolution of approximately 10 μm. While a scanning approach can be used to observe localized features, it has poor temporal resolution. One commercial instrument (7) specifies 4 s per point, corresponding to 11 h for acquisition of a 100 × 100 pixel image. Hurd and Brinker (8, 9) have devised an imaging system that tracks several discrete nulls for drying sol gel films. Useful spatial information is obtained from this method, however, it does not yield a quantitative full field ellipsometric analyses of the illuminated area since not all regions of the drying film satisfy the null conditions.

Recently, Cohn *et al.* (10-15) developed dynamic imaging microellipsometry (DIM). In contrast to the Hurd and Brinker (8, 9) technique, DIM is a radiometric full field imaging approach to ellipsometry. Good spatial resolution (approximately 20 μm) and precision in addition to good temporal resolution (minutes) was demonstrated. The DIM approach utilized the standard polarizer, specimen, compensator, analyzer (PSCA) ellipsometry configuration in combination with an imaging lens, a charge-coupled device (CCD) video camera, and digital image processing techniques to acquire high spatial resolution ellipsometric data with good temporal resolution.

* Electrochemical Society Student Member.
** Electrochemical Society Active Member.

The purpose of this paper is to report on the latest DIM system and to demonstrate the usefulness of this technique for examining passive film growth on materials with microstructural inhomogeneities. Results are reported for passive film growth on a polycrystalline iron sample and an aluminum tantalum alloy that contained intermetallic precipitates.

Dynamic Imaging Microellipsometry Theory and System Design

A block diagram of the DIM system used in this study is illustrated in Fig. 1. The conventional PSCA optics are used in combination with a 105 mm Nikkor imaging lens and a Pulnix TM-34K CCD video camera in the focal plane. A half-wave plate mounted in an Oriel computer controllable rotation stage is inserted after the polarizer and is used to rotate the plane of the linearly polarized light while the polarizer remains fixed (12). A Hewlett Packard HLMP-8150 ultrabright light emitting diode was used as the light source and provided quasimonochromatic light of wavelength 650 nm. The ultrabright diode was used instead of a laser source to eliminate the speckle interference associated with highly monochromatic light (16).

An analytical description of the system was derived utilizing the Jones matrix and vector formalisms (11, 12). The intensity at the CCD detector for a given initial polarization angle is described as follows

$$I(P) = \frac{G^2}{2}\{a\cos^2 P\tan^2\psi + b\sin^2 P + (c\cos\Delta - d\sin\Delta)\sin 2P\tan\psi\} \quad [1]$$

where

$$a = 1 + \cos 2C\cos 2(A - C)$$

$$b = 1 - \cos 2C\cos 2(A - C)$$

$$c = \sin 2C\cos 2(A - C)$$

$$d = \sin 2(A - C)$$

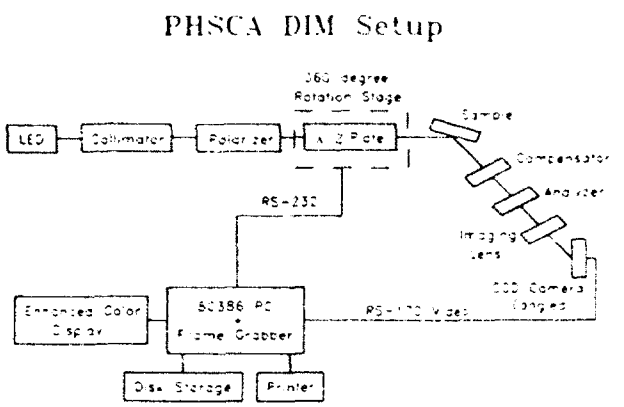

Fig. 1. Schematic illustration of the PHCSA (polarizer, half-wave plate, specimen, compensator, analyzer) DIM setup. Note that the backbone of the setup is similar to the traditional PSCA (polarizer, specimen, compensator, analyzer) configuration.

G is the system gain (related to the optical components), A and C are the analyzer and compensator azimuth angles, respectively, and Δ and ψ are the ellipsometric parameters of interest. The parameter Δ is the change in phase and tan ψ the change in relative amplitude between the orthogonal components of the electric field vector of the incident light. Since Eq. [1] contains three unknowns (Δ, ψ, and G) it is not directly solvable. The approach taken involves digitizing a minimum of three intensity images, each at a unique initial polarization angle. The independent equations obtained are then used to solve directly for Δ and ψ. A four-image algorithm where images are captured at initial polarization states of -45°, 0°, 45°, and 90° is shown below and was used for computational ease in this study

$$\Delta = \cos^{-1}\left(\frac{I(45°) - I(-45°)}{2\sqrt{I(0°)I(90°)}}\right) - \tan^{-1}\left(\frac{d}{c}\right) \qquad [2]$$

$$\psi = \tan^{-1}\left(\sqrt{\frac{I(0°)}{I(90°)}}\sqrt{\frac{b}{a}}\right) \qquad [3]$$

Δ and ψ maps are calculated point by point from the digitized intensity images recorded at the four initial polarization states [$I(-45°)$, $I(0°)$, $I(45°)$, and $I(90°)$] using Eq. [2] and [3]. The Δ and ψ maps are hereafter referred to as ellipsograms. A sample ellipsogram of a silicon wafer is illustrated in Fig. 2. Note that the gray levels observed are linearly proportional to Δ and ψ. The wafer is covered with an SiO_2 film that has a gradient in thickness from approximately 30 to 50 nm owing to nonuniform growth conditions. The variation in film thickness from the upper left corner to the lower right corner is easily observed in the figure.

The system was automated by a personal computer with an 80386 microprocessor, an 80387 math coprocessor, and a Data Translations DT2862 Arithmetic Frame Grabber that digitizes 480 video lines with 512 pixels in each line. Data acquisition and processing utilized the algorithm described in Eq. [2] and [3]. The software also enabled ellipsograms to be computed using two distinct three image algorithms reported by Cohn (15). Acquisition time for three images is approximately 7.5 s, while for four images 10.75 s is required. Ellipsogram to ellipsogram temporal resolution for the three and four image algorithms are 20 and 21 s, respectively. Temporal resolution for the present system is limited by the rotation speed of the half-wave plate.

Experimental

Polycrystalline iron parameters.—A 99.99% pure iron sample with grains that were up to 2 mm in diameter was examined via DIM. All measurements were made in a pH 7.2 sodium borate-boric acid buffer solution. The specimens were prepared by abrading through 4000 grit paper. The final surface polish was performed with a 0.25 μm diamond aerosol spray. Prior to anodic polarization the sample was polarized to -950 mV SCE to remove the air formed oxide. The specimen was then polarized to 500 mV SCE for nearly 5 h. Formation of the passive film was monitored via DIM. Ellipsograms were acquired at 60 s intervals for the first 13 min, 10 min intervals for the following 90 min and 30 min intervals for the final 3 h. The ellipsometric parameters, Δ and ψ, were monitored for various grains during passive film growth and plotted vs. log time. An approximate orientation of several of the grains of interest was determined by SEM examination following etching in a 10% Nital solution. The Nital solution preferentially attacks the iron exposing (100) planes (17).

Aluminum tantalum alloy parameters.—A section from an Al-1 atom percent (a/o) Ta alloy prepared via dynamic compaction of atomized alloy powders was analyzed via DIM. Scanning electron microscopy (SEM) characterization of the alloy showed aluminum tantalum [probably Al_3Ta (18)] precipitates up to 20 μm in diameter as illustrated in Fig. 3. As a result this alloy provided an excellent control sample for determination of spatial resolution of DIM in solution. All measurements were made in a pH 7.2 sodium borate-boric acid buffer solution. The specimen surfaces were prepared by dry abrading the specimen through 4000 grit paper. Abrasion was carried out under dry conditions to avoid galvanic interactions between the precipitates and the matrix material. The final surface polish was performed using a 0.25 μm diamond aerosol spray. SEM analysis showed no visible galvanic attack during the polishing. It should be noted, however, that, even after polishing, these alloys had a surface roughness or texture of

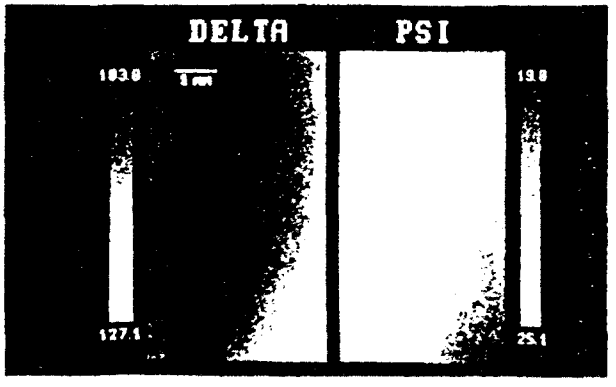

Fig. 2. Sample ellipsogram of silicon wafer with an SiO_2 film that varies in thickness from approximately 30 to 50 nm. The gray scale of the images is directly proportional to Δ and ψ. The scales provide the values for Δ and ψ.

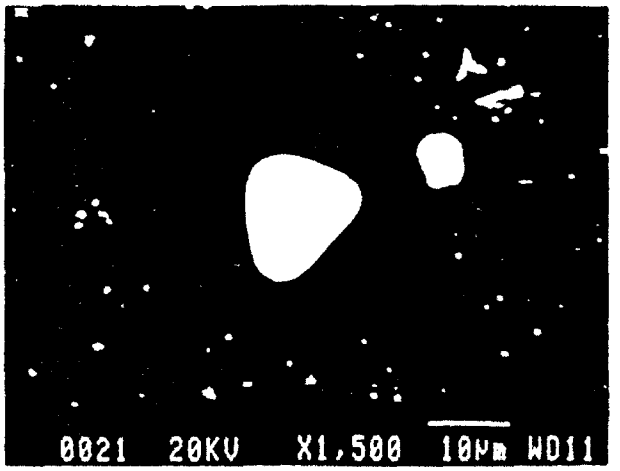

Fig. 3. Photomicrograph of aluminum tantalum precipitate in Al-1 a/o Ta alloy. The dark region around the precipitate is probably a dealloyed region.

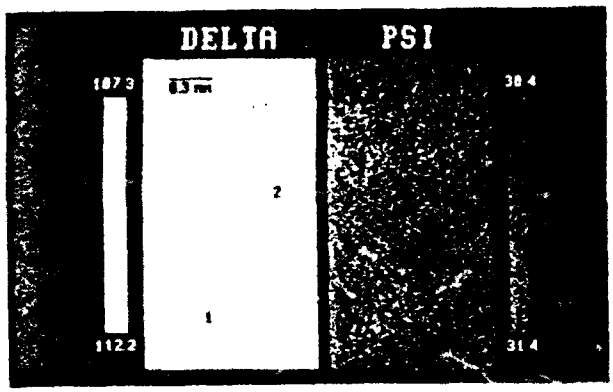

Fig. 4. Ellipsogram for iron after 5 h polarization at 500 mV SCE in a borate buffer solution. Note that the grains can be "observed" in the Δ map but not in the ψ map indicating passive film thickness differences from grain to grain.

the order of 10s of microns resulting from the dynamic compaction forming technique. This provided difficulties in the ellipsometric analysis and will be discussed later. The polarization behavior of this alloy was determined via potentiodynamic polarization scans. The alloy was scanned from open circuit (approximately −980 mV SCE) to 1200 mV SCE at a scan rate of 0.2 mV per second. Ellipsograms were acquired at 400 mV intervals during the scan.

Results and Discussion

Polycrystalline iron.—Figure 4 is an ellipsogram of the polycrystalline iron sample acquired after 5 h of polarization at 0.5 V SCE. Recall that Δ and ψ are linearly proportional to the gray levels in their respective maps. Note that the grain structure of the sample is "observable" in the Δ map but not in the ψ map, indicating differences in the passive film thickness over the respective grains. If the difference observed were only owing to surface roughness, the grain structure would also be "observable" in the ψ map since ψ is sensitive to roughness (19). It should also be pointed out that orientation effects are minimized when the film is reduced providing further support that the grain structure "observed" in Fig. 4 is the result of film thickness differences.

Figure 5 is a plot of the change in Δ *vs.* log time for the grains labeled 1 and 2 in Fig. 4 at 0.5 V SCE. Negative "δΔ" is linearly proportional to change in film thickness for small film thickness (20). Therefore Fig. 5 illustrates that the growth of the passive film is dependent on the orientation of the substrate. Grain 1 in Fig. 4 is close to a (111) orientation while grain 2 is close to (100) as determined by examination of etched surfaces in an SEM. Neither grain was oriented precisely. Using McCrackin's program (21), it was determined that the final difference in film thickness between the two grains was approximately 0.4 nm. The final thickness for grain 2 was approximately 3.6 nm compared to approximately 3.2 nm for grain 1. Dependence of film growth rate on grain orientation on iron has been observed by Kruger and Calvert (22) by comparing measurements made on single crystals. Orientation effects were expected since the passive film on iron is known to be crystalline (23-25). DIM enables the effects of microstructure on the growth of the passive film on iron to be directly observed on a polycrystalline sample. The DIM technique is well suited to studying surface phenomenon, such as passive film growth, that are dependent on grain orientation.

Similar measurements have been performed on a 99.999% pure polycrystalline aluminum sample. No dependence on orientation of passive film growth was observed. This is not surprising since the passive films on aluminum have been shown to be amorphous (26).

Aluminum tantalum alloys.—Aluminum alloys containing solid solution additions of tantalum exhibit a markedly increased resistance to pitting corrosion (27, 28). The improvement, however, is degraded by the presence of intermetallic precipitates (29) such as those observed in the dynamically compacted alloy used in this study. Determination of the properties of the passive film over the precipitates would aid in understanding the breakdown processes of these alloys. The polarization behavior of the dynamic compacted Al-1.0 a/o Ta alloy in pH 7.2 borate buffer solution is illustrated in Fig. 6. The increase in current at approximately 1100 mV SCE is owing to the onset of O_2 evolution. This result was surprising since on pure aluminum the O_2 evolution reaction is not observed. Neither is it observed on solid solution Al-8 a/o Ta in the same electrolyte (30). In addition, Frankel *et al.* (28) observed pitting potentials of 1600 mV SCE for an Al-41 a/o Ta solid solution alloy in 0.1*M* NaCl and reported no O_2 evolution prior to breakdown. Another aluminum alloy with 10 a/o solid solution additions of tungsten rather than tantalum exhibited pitting potentials of nearly 2000 mV SCE in 0.1*M* NaCl and also reported no O_2 evolution prior to breakdown (31). Since the O_2 evolution reaction is not observed on solid solution Al-Ta and Al-W alloys nor on pure aluminum or a solid solution Al-8 a/o Ta alloy in a pH 7.2 borate buffer solution containing no Cl^-, it is concluded that the reaction occurs at the precipitates in the alloy used in this study. Further evidence is supplied by SEM and XRM analysis of the dyamically compacted alloys that shows no evidence of impurities that might act as sites for O_2 evolution.

As stated in the Experimental section surface preparation was difficult. Repeated attempts at producing an opti-

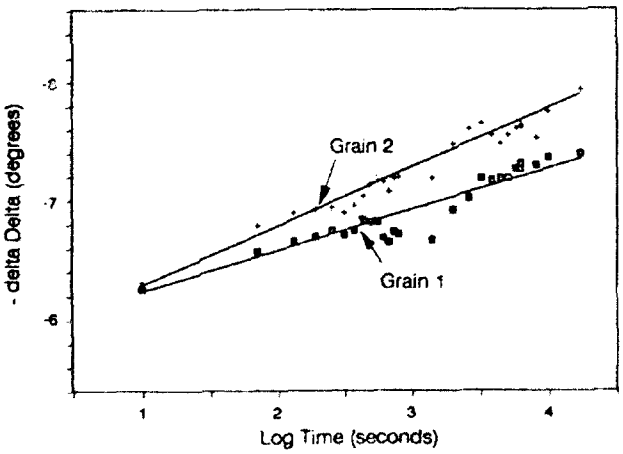

Fig. 5. δΔ *vs.* log time for the grains labeled 1 and 2 in Fig. 4. −δΔ is proportional to film thickness. The growth kinetics for the film over grain 1 are more rapid than that over grain 2. The final thickness of the film over grain 1 is approximately 0.5 nm thicker than the film over grain 2.

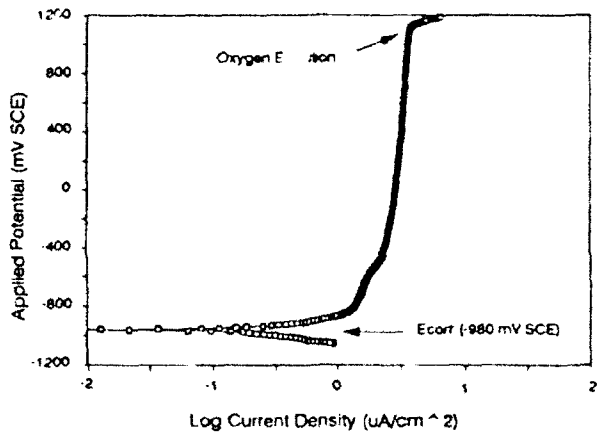

Fig. 6. Polarization curve for Al-1 a/o Ta alloy in pH 7.2 borate buffer solution. The increase in current at approximately 1100 mV SCE is the result of O_2 evolution. O_2 evolution occurs on the aluminum tantalum precipitates similar to those shown in Fig. 3.

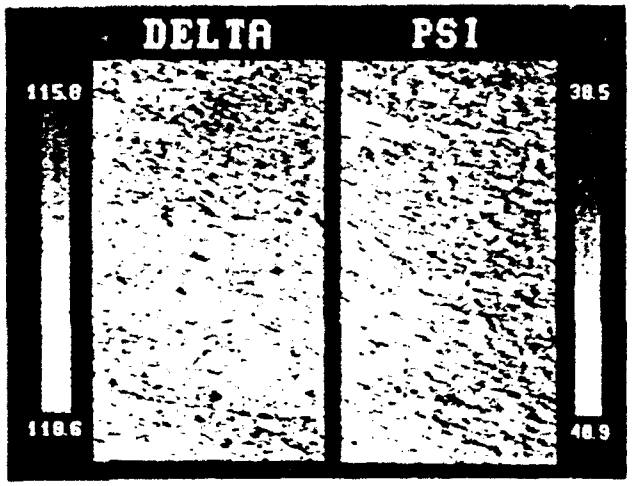

Fig. 7. Ellipsogram of Al-1 a/o Ta alloy at E_{corr} (−980 mV SCE). Note the spatial noise in the Δ and ψ maps that results from the surface roughness of these alloys.

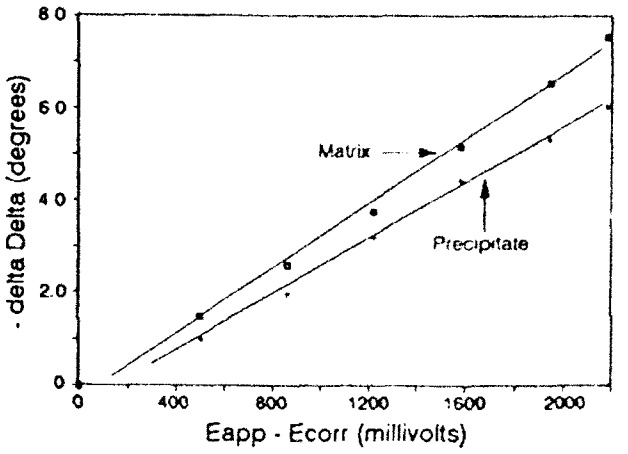

Fig. 9. (−δΔ) vs. applied potential for the precipitate and matrix material in the Al-1 a/o Ta alloy. A thinner passive film over the precipitate at a given applied potential is implied.

cally flat surface on these specimens failed. The textured surfaces resulted in textured ellipsograms and interfered with locating and ellipsometrically analyzing the intermetallic precipitates in these alloys. Figure 7 is an ellipsogram of the alloy at E_{corr} that demonstrates the effects of the surface texture on the ellipsometric data. Spatial variations of several degrees in Δ and ψ are evident. It should be pointed out, however, that Fig. 7 demonstrates that the DIM technique provides a method for examining surface roughening *in situ*.

Despite the severity of the surface roughness, precipitates were observed and qualitatively analyzed ellipsometrically. To locate the precipitates the sample was first polarized to 2000 mV SCE and held at that potential until O_2 bubbles formed on the surface. As described above, it was concluded that the O_2 evolution reaction occurs at the precipitates. After digitally locating the bubbles the previously generated ellipsograms were analyzed in the regions where bubbles formed. Figure 8 illustrates what was observed ellipsometrically in these locations. The right side of the figure is a polarized light photograph of the region around one of the bubbles. The bubble appears as a doublet because it shades both the incident and reflected beam. The left side of the figure is a Δ map of the same region. Note the dark area in the center of the box, corresponding to a lower value of Δ for that region. This region is the Δ value over one of the precipitates in the alloy. The size of the region is approximately 20 μm. At the magnification used each pixel is approximately 4-5 μm square. At E_{corr} (−980 mV SCE) where the passive film is thin, the Δ measured for the precipitate is approximately 3 degrees less than that for the matrix. It was also observed that ψ was approximately 1.5 degrees higher for the precipitate than over the matrix. This probably results from different refractive index values for the substrate.

Fig. 8. Δ map (left) and polarized light photograph (right) of Al-1 a/o Ta alloy. The Δ map was computed after polarization at 1200 mV SCE. The photograph was acquired after polarization at 2000 mV SCE which promoted bubble formation over aluminum tantalum precipitates from O_2 evolution. One such bubble is observed. The "dark spot" in the box on the Δ map indicates that the Δ value for the precipitate is less than that for the matrix material.

Figure 9 plots (−δΔ) *vs.* applied potential for the precipitate and the matrix material. Note that the slope of (−δΔ) *vs.* applied potential for the precipitate is less than that of the matrix, indicating that to a first approximation the precipitate forms a thinner film at a given applied potential than the matrix. Consideration of the film indexes lends further support to this conclusion. Muth (32) measured an index of 2.22 for Ta_2O_5. The index of Al_2O_3 is 1.65 (33). He also measured a film index of 2.12 for an Al-73 a/o Ta alloy. Therefore it is expected that the index of the precipitate passive film to be between that of pure Ta_2O_5 and pure Al_2O_3, hence an index that is higher than that of Al_2O_3. This supports the contention that the precipitate passive film is thinner than the matrix passive film since forming a passive film with a greater index results in a greater decrease in Δ for a given film thickness. Therefore, even if the slopes were identical in Fig. 9 it would indicate a thinner film on the precipitate. Assuming an index of 1.79 for the passive film on Al_3Ta (based on a law of mixtures approximation) and an index of 1.65 for the passive film on the matrix (the same for the passive film on aluminum), a final matrix passive film thickness of approximately 7.0 nm and a final precipitate passive film of approximately 4.5 nm were calculated. This may result in an incompatibility between the two films causing local strains or flaws such as dislocations that promote Cl^- ingress and degrade the protective nature of the passive film. The role of defects in the breakdown of aluminum is controversial and has been discussed considerably [see review by Foley (34)]. Quantitative comparison of the films over the precipitate and matrix is difficult owing to the surface roughness of the alloy. The purpose here is instead to demonstrate that features of the order of 20 μm are observable ellipsometrically (even on a specimen that is far from ideal) and that determination of passive film parameters on these features is possible in solution. In future experiments, sputtered alloys that are optically flat and smooth [similar to those described previously (27, 31, 35)] will be examined. This will decrease spatial noise significantly and enable better evaluation of the passive films and their dependence on microstructure.

Conclusions

This paper reports on the latest DIM system and demonstrates the usefulness of the DIM technique for *in situ* ex-

amination of passive film growth on materials with microstructural inhomogeneities. On polycrystalline iron it was shown that the thickness and growth kinetics of the passive film were dependent on the grain orientation. Grain to grain thickness variations of less than 1 nm were easily observable. The in situ spatial resolution of the DIM technique was determined via examination of a dynamically compacted Al-1 a/o Ta alloy that contained intermetallic precipitates up to 20 μm in diameter. Despite the high degree of surface roughness on these samples, precipitates were located and qualitatively analyzed. The precipitates were observed to form a thinner passive film as a function of applied potential than the matrix material. The incompatibility between the film over the precipitate and that over the matrix may effect the pitting behavior of the alloys.

Acknowledgments

This research was supported by the Office of Naval Research Contract No. N00014-89-J-1180. The authors are grateful to Dr. John Sedricks for his role in providing this support. One of the authors (C.C.S.) was supported throughout this work by a National Science Foundation Award. The aluminum tantalum alloy specimens were donated by Martin Marietta Laboratories. Gene Danko is acknowledged for providing the silicon wafer.

Manuscript submitted July 1, 1991; revised manuscript received Nov. 6, 1991. This was Paper 64 presented at the Washington, DC, Meeting of the Society, May 5-10, 1991.

The Johns Hopkins University assisted in meeting the publication costs of this article.

REFERENCES

1. R. M. A. Azzam and N. M. Bashara, "Ellipsometry and Polarized Light," Elsevier Sci. Pub., New York (1987).
2. J. Kruger, *J. Physique*, **38**, Colloq. C-5, Suppl. to No. 11, CS 129-CS 138 (1977).
3. D. J. Dunlavy, R. B. Hammond, and R. K. Ahrenkiel, Los Alamos National Labs Report LA-UR-81-1806, 6p (1981).
4. K. Sugimoto and S. Matsuda, *This Journal*, **130**, 2323 (1983).
5. K. Sugimota, S. Matsuda, Y. Ogiwara, and K. Kitamura, ibid., **132**, 1791 (1985).
6. M. Erman and J. B. Theetan, *J. Appl. Phys.*, **60**, 859 (1986).
7. "Auto Gain Ellipsometers," Bulletin EE, Gaertner Scientific Corporation, p. 13.
8. A. J. Hurd and C. J. Brinker, *J. Physique*, **49**, 1017 (1988).
9. A. J. Hurd and C. J. Brinker, in "Better Ceramics through Chemistry III," Brinker, Clark and Ulrich, Editors, Materials Research Society (1988).
10. R. F. Cohn, J. W. Wagner, and J. Kruger, *This Journal*, **135**, 1033 (1988).
11. R. F. Cohn, J. W. Wagner, and J. Kruger, *Appl. Opt.*, **27**, 4664 (1988).
12. R. F. Cohn and J. W. Wagner in "Review of Progress in Quantitative NDE," Vol. 8B, D. O. Thompson and D. E. Chimenti, Editors, p. 1219, Plenum Press, New York (1989).
13. R. F. Cohn and J. W. Wagner, in "Proceedings of the Society for Photo-Optical Instrument Engineering," 1036, 125, SPIE (1989).
14. R. F. Cohn and J. W. Wagner, *Appl. Opt.*, **28**, 3187 (1989).
15. R. F. Cohn, ibid., **29**, 304 (1990).
16. R. T. Allemeier and J. W. Wagner, in "Review of Progress in Quantitative NDE," Vol. 10A, D. O. Thompson and D. F. Chimenti, Editors, Plenum Press, New York (1990).
17. R. L. Anderson, Scientific Paper 425-C000-CP2, Westinghouse Research Laboratories (1961).
18. G. D. Davis, T. L. Fritz, B. J. Rees, B. A. Shaw, and W. C. Moshier, Martin Marietta Laboratories Annual Report, MML TR 91-10c (1991).
19. T. Smith, *Surf. Sci.*, **56**, 252 (1976).
20. J. Kruger and P. C. S. Hayfield, in "Handbook on Corrosion Testing and Evaluation," W. H. Ailor, Editor, John Wiley & Sons, Inc., New York (1971).
21. F. L. McCrackin, "A Fortran Program for Analysis of Ellipsometer Measurements," NBS Tech. Note 479 (1969).
22. J. Kruger and J. P. Calvert, *This Journal*, **114**, 43 (1967).
23. M. Nagayama and M. Cohen, ibid., **109** 781 (1962).
24. F. C. Ho and J. L. Ord, ibid., **119**, 139 (1972).
25. J. L. Ord and D. J. De Smet, ibid., **123**, 1876 (1976).
26. J. S. L. Leach and B. R. Pearson, *Corros. Sci.*, **28**, 43 (1988).
27. G. D. Davis, W. C. Moshier, T. L. Fritz, and G. O. Cote, *This Journal*, **137**, 422 (1990).
28. G. S. Frankel, M. A. Russak, C. V. Johnes, M. Mirzamaani, and V. A. Brusic, ibid., **136**, 1243 (1989).
29. G. D. Davis, W. C. Moshier, T. L. Fritz, G. O. Cote, G. G. Long, and D. R. Black, Martin Marietta Laboratories Annual Report, MML TR 89-12c (1989).
30. C. C. Streinz, *This Journal*, In press.
31. B. A. Shaw, T. L. Fritz, G. D. Davis, and W. C. Mosier, ibid., **137**, 1317 (1990).
32. D. G. Muth, *J. Vac. Sci. Technol.*, **6**, 749 (1969).
33. R. M. Goldstein, R. J. Lederich, and F. W. Leonhard, *This Journal*, **117**, 503 (1970).
34. R. T. Foley, *Corrosion*, **42**, 277 (1986).
35. W. C. Mosier, G. D. Davis, J. S. Ahearn, and H. F. Hough, *This Journal*, **134**, 2677 (1987).

Reprinted from JOURNAL OF THE ELECTROCHEMICAL SOCIETY
Vol 139, No 4, April 1992
Printed in U.S.A.

A Novel Method for Generating Quantitative Local Electrochemical Impedance Spectroscopy

R. S. Lillard

Department of Materials Science and Engineering, The Johns Hopkins University, Baltimore, Maryland 21218

P. J. Moran

Department of Mechanical Engineering, United States Naval Academy, Annapolis, Maryland 21402

H. S. Isaacs

Department of Applied Science, Brookhaven National Laboratory, Upton, New York 11973

ABSTRACT

A local electrochemical impedance spectroscopy (LEIS) technique for mapping the ac impedance distribution, as a function of frequency, of an electrode has been developed. In LEIS, as in traditional ac impedance methods, a sinusoidal voltage perturbation between the working and reference electrode is maintained by driving an ac current between the working electrode and a distant counterelectrode with a potentiostat. Local ac impedances are then derived from the ratio of the applied ac voltage and the local ac solution current density. The local ac current density is obtained from potential difference measurements near the electrode surface using a probe consisting of two micro-electrodes. By measuring the ac potential difference between the micro-electrodes, and knowing their separation distance and the solution conductivity, the local ac solution current density is derived. The accuracy of the local ac impedance data generated with this technique was established by investigating two model systems. The first provided a homogeneous electrode which allowed LEIS measurements to be compared to traditional EIS, while the second system provided a heterogeneity of known size and location whose components were easily characterized with traditional techniques. It is shown that area-normalized scanning ac impedance measurements of the homogeneous electrode agreed well with traditional results. In addition, because LEIS maps the impedance properties of an electrode, the defect in the heterogeneous electrode was easily detected, while traditional ac impedance of this electrode gave little indication of its presence.

Background and Approach

AC impedance (also known as electrochemical impedance spectroscopy, (EIS)) is a powerful nondestructive *in situ* technique which has been used extensively to investigate electrochemical systems (1-4). In the conventional EIS approach, a small sinusoidal voltage perturbation is applied across the electrochemical interface. Impedance data for the whole electrode is then generated by measuring the ratio of the voltage perturbation and its current response as a function of frequency. The impedance is most commonly presented in either Nyquist format ($Z_{imaginary}$ *vs.* Z_{real}) or Bode plots ($|Z|$ *vs.* ω and θ *vs.* ω). However, because the current response of the whole electrode is used to generate impedance data, a surface averaged measurement results, which can lead to difficulties when interpreting data if the behavior is not uniform over the entire electrode interface; as is the case in localized corrosion systems. The nonuniformity arises because the frequency dependence of the current distribution in the vicinity of a corrosion site is markedly different from that near an inactive, or passive area (5).

Although EIS has been applied to localized corrosion systems, data analysis for these systems is complex (6-9). For this reason, to investigate localized corrosion due to multi-phases, grain boundary effects, or other surface heterogeneities which may occur on an electrode surface, a method of generating local ac impedance data is preferable.

DC scanning techniques.—Several scanning techniques have been developed for the *in situ* examination of dc currents associated with localized corrosion and surface heterogeneities. The most common is the scanning vibrating electrode technique (SVET) (10). In SVET a "micro-tip" probe for measuring the current distribution in solution, is constructed from a thin (less than 20 μm) platinum wire insulated except at the tip. The wire is mounted on a bimorph piezoelectric reed which vibrates the tip normal to the electrode at a characteristic frequency. For areas on the electrode where there is a net uniform anodic or cathodic current, the dc potential in solution above the electrode will be proportional to distance from the electrode. By oscillating the platinum probe in this potential gradient an induced ac voltage will result. This induced ac signal can be measured precisely with a lock-in amplifier referenced to the oscillation (vibration) frequency of the piezoelectric. The dc current distribution in solution above the electrode has been mapped with this vibrating probe by scanning it at a distance less than 50 μm above the electrode with an X-Y translation stage (10-14).

While the SVET has been used successfully to investigate the initiation of stress corrosion cracking (11), surface heterogeneities (12), and galvanic corrosion (13, 14), its application is limited to systems which are electrochemically active; i.e., dc currents must flow in solution.

Recent attempts to develop scanning ac impedance systems.—Isaacs and Kendig (15), as well as other investigators (16, 17), have combined scanning technology with impedance methods in an attempt to generate local ac impedance data for discrete areas on electrodes.

In these techniques, the electrode to be examined was polarized locally with a small disk shaped probe that contained "micro" reference and counterelectrodes. In an attempt to confine the current generated by the local polarization to the area of interest, a thin layer cell geometry was employed. This was accomplished by maintaining a distance of 30 μm between the disk shaped probe and electrode surface. While this technique has been used to generate qualitative results, no quantitative local ac impedance

data has been produced with this method. In addition, the use of a thin layer cell geometry may markedly influence the natural corrosion process, by altering mass transport, for example. The thin layer cell's effectiveness in confining the current density distribution to a local area also depends vastly on the impedance properties of the electrode.

A novel method of generating local ac impedance data.—This paper presents a novel method for generating quantitative local ac impedance data. The technique is founded on the premise that the ac solution current densities very near the working electrode, in a conventional three electrode ac impedance measurement, are proportional to the local impedance properties of the electrode.

Other investigators have demonstrated that the current distribution very near an electrode may be mapped in three dimensions; each, or any combination of which may be mapped for an electrode surface by choosing the correct probe geometry (18-20). To simplify data analysis, this study has chosen to measure only the component of the ac current normal to the electrode. Because current and potential lines are perpendicular to one another, to measure the ac solution current density normal to the electrode it is necessary to measure the ac potential drop between planes parallel to the electrode. Further, to effectively map the local impedance properties of an electrode, this ac potential drop measurement must be made on a relatively small scale. To accomplish this a two electrode micro-probe, shown in Fig. 1, was designed.

To obtain the local ac solution current density at the tip of the probe, first the ac potential difference between the two probe electrodes is measured with a frequency response analyzer or lock-in analyzer. The ac solution current density at the probe tip is obtained from this potential measurement by using the following relationship which is derived from Ohm's law

$$i(\omega)_{local} = \frac{\Delta V(\omega)_{probe} \cdot \sigma}{l} \qquad [1]$$

where $i(\omega)_{local}$ is the local ac solution current density, $\Delta V(\omega)_{probe}$ is the ac potential difference at the probe, σ is the solution conductivity, and l is the separation distance between the tip "micro-openings" in units of amps/cm², V, $(\Omega\ cm)^{-1}$, and cm, respectively. The magnitude of the local impedance is derived from Eq. [1]

$$|Z(\omega)|_{local} = \frac{V(\omega)_{applied}}{\Delta V(\omega)_{probe}} \frac{l}{\sigma} \qquad [2]$$

where $V(\omega)_{applied}$ is the magnitude of the applied voltage perturbation between the reference and working electrodes, which is an area normalized local impedance value, in units of $\Omega\ cm^2$. It should be noted in the derivation of $|Z(\omega)|_{local}$ that the ac solution current density at the probe tip (Eq. [1]) is assumed to be equal to the current density at the electrode surface, i.e., all of the ac current at the tip is assumed to be traveling normal to the electrode. The validity and implications of this assumption shall be addressed in the Discussion section of this paper.

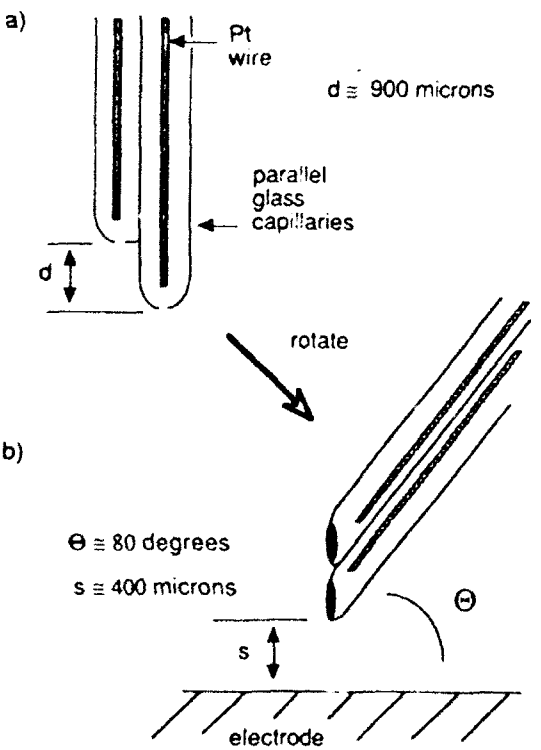

Fig. 1. A diagram of the bi-electrode probe used to make local ac impedance measurements.

Experimental

Probe design.—The bi-electrode probe used in these experiments to measure the component of the ac solution current density normal to the electrode is shown in Fig. 1a and b. It was constructed by drawing down two parallel and attached glass capillaries with an initial inside diameter of 1.0 mm, to a final inside diameter of approximately 0.10 mm. As shown in Fig. 1, these "micro-openings" were displaced (with respect to the plane of the electrode) both vertically and horizontally by 0.85 ± 0.050 and 0.30 ± 0.050 mm, respectively. Into each of these glass tubes, a thin platinum wire, approximately 0.225 mm in diam, was inserted. To reduce the interfacial impedance of these platinum electrodes, each wire was platinized by cathodic polarization in 2% chloroplatinic acid at a density of approximately 100 mA/cm² for approximately 5 min (21). To measure the normal component of the current, this probe was held at approximately an 80 ± 1 degree angle with respect to the electrode so that the openings would be aligned normal to the electrode, along the Z axis. This configuration, shown in Fig. 1b, provided a final probe separation distance along the Z axis of approximately 0.9 mm.

Electrochemical and scanning apparatus.—A Solartron 1286 Electrochemical Interface was used to control the dc potential of the test electrodes and apply the ac sinusoidal voltage perturbation generated by a Solartron 1255 Frequency Response Analyzer (FRA). Because the probe impedances were high relative to the input impedance of the FRA (approximately $3 \times 10^5\ \Omega$ vs. $1 \times 10^6\ \Omega$, respectively) direct measurement of the probe signal with the Solartron 1255 FRA resulted in an attenuation of the true potential difference between the probe electrodes. In addition, an impedance mismatch between the two electrodes created a high common mode voltage at the probe electrode. The combination of these two effects prevented accurate measurement of the ac potential difference between the probe electrodes when made directly with the Solartron FRA.

To overcome these problems, the probe signal was first buffered with a high input impedance, high common mode rejection ratio, and low output impedance ($1 \times 10^9\ \Omega$, 1×10^6 and $<1\ \Omega$, respectively) Analog Devices AD-625 linear output instrumentation amplifier. The instrumentation amplifier also permitted the input signal to be amplified by as much as 1000 ×, allowing very small potential differences between the probe electrodes to be easily measured with the Solartron FRA. Further information on this instrumentation is available elsewhere (19).

To generate ac impedance maps of electrodes with the probe, a high resolution, high accuracy scanning system was assembled. To avoid unnecessary vibration of the probe, which may have resulted in an error in the measurements, the scanning system was designed to move the electrode, in a specially designed cell, below the probe which was held stationary. Movement of the cell in the X and Y directions was accomplished by mounting two Aerotech ATS210 Accudex stages orthogonally to one another. Each of these stages was driven by Aerotech 101SM-DM4005 stepper motors. This scanning system has a resolution of 1 μm and an accuracy of 2.5 μm/25 mm.

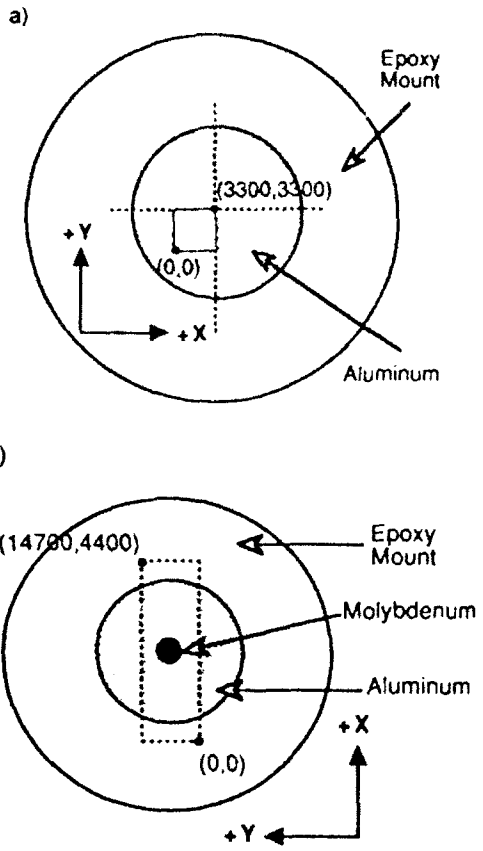

Fig. 2. Diagrams of the model electrodes including the area examined with the scanning EIS technique a) the aluminum electrode b) the aluminum/molybdenum electrode.

Because it is somewhat impractical to manually control the FRA, potentiostat, and motion controller while simultaneously recording data during an experiment, a computer data acquisition system and the necessary software was developed and is discussed in detail elsewhere (19).

Model electrodes and experimental parameters.—To demonstrate the validity of the experimental method, a homogeneous, or uniform, electrode surface consisting of a single phase high purity material was first tested in an electrolyte which did not produce localized corrosion. The electrode for this experiment, presented in Fig. 2a, was a 2.25 cm diam 99.999% aluminum cylinder mounted in epoxy and was studied in a 0.5*M* boric acid/0.05*M* sodium borate buffer solution (pH = 7.2, $\sigma = 5.32 \times 10^{-3}\ \Omega^{-1} \cdot cm^{-1}$) to keep it free of localized corrosion.

To demonstrate that the technique was sensitive to surface heterogeneities, a second electrode was designed. The electrode was constructed by force molding a 99.999% pure aluminum sample around a 0.127 cm diam molybdenum wire; the final outside diameter of the electrode being 1.27 cm. This electrode was mounted in epoxy and a diagram of it is presented in Fig. 2b.

In all scanning ac impedance measurements, a 30 mV rms sinusoidal voltage perturbation was potentiostatically maintained between the test electrode and a saturated calomel reference electrode (SCE). An applied dc potential of −0.675 V *vs.* SCE was also maintained between the test and reference electrodes. For the Al/Mo electrode this dc potential is approximately 100 mV cathodic to E_{corr}, while for the 99.999% Al electrode this dc potential was approximately 35 mV anodic to E_{corr}. Impedance maps were generated for the Al/Mo electrode in the frequency range of 4.64 to 4677 Hz while for the 99.999% Al electrode ac impedance maps were generated over a frequency range of 2.51 to 6310 Hz.

Because each electrode was symmetric about its center, it was only necessary to map a small section of each, as presented in Fig. 2 a and b. For the Al/Mo electrode this area was approximately 0.65 cm² (1.47 cm × 0.44 cm) and was mapped by stepping the electrode below the probe in the X and Y directions in increments of 0.070 and 0.040 cm, respectively. The scan area of the 99.999% Al electrode was approximately 0.11 cm² (0.33 × 0.33 cm) and was mapped by stepping the electrode below the probe in the X and Y directions in increments of 0.030 and 0.030 cm.

To evaluate the scanning ac impedance measurements, traditional ac impedance experiments were performed on the Al/Mo electrode and 99.999% Al electrodes used in the scanning experiments as well as on a 99.95% molybdenum electrode. These experiments were also carried out in the same boric acid/sodium borate buffer solution and at the same applied dc potential (−0.675 V *vs.* SCE) and were conducted with a Princeton Applied Research Electrochemical Impedance System and 378 Software. The ac voltage perturbation used for these experiments was 10 mV rms and 5 data points per decade of frequency were recorded over a frequency range of 1×10^{-3} to 1×10^{5} Hz.

Prior to all impedance experiments, each electrode surface was first polished with successively finer grits of silicon carbide paper finishing with 4000 grit. The surfaces were then further polished on a polishing wheel with diamond spray, the final grit size being 1 μm. After polishing, the sample was washed and then degreased with methanol and ethanol and left in the laboratory air for periods between 6 and 24 h before immersion in the test solution.

Results

Traditional ac impedance experiments.—Before analyzing the ac impedance maps of the 99.999% aluminum and aluminum/molybdenum electrodes, it will be helpful to first examine the data from traditional ac experiments performed on the aluminum, molybdenum, and the Al/Mo electrodes. The results of these experiments are presented in the form of Bode magnitude and Bode phase plots in Fig. 3a and b, respectively, for later reference. It may be

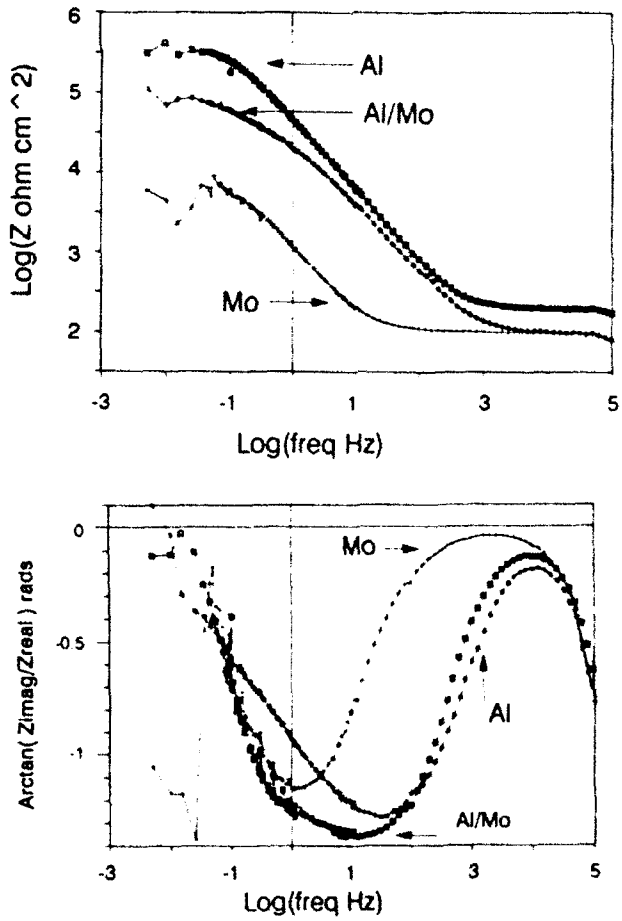

Fig. 3. Traditional EIS data for bulk aluminum, bulk molybdenum, and aluminum/molybdenum electrodes a) Bode magnitude plot b) Bode phase plot.

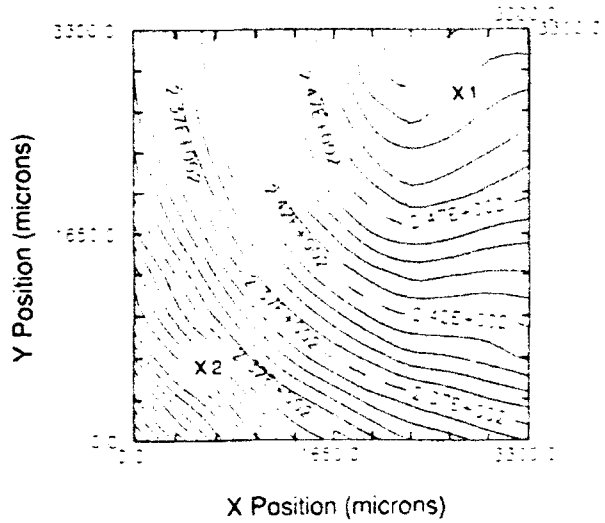

Fig. 4. A map of the magnitude of the impedance (in contour) of the aluminum electrode at 6310 Hz generated with the scanning impedance technique. Each contour line represents 1.0 Ω cm².

noted that some of the low frequency data in these plots, below 10^{-1} Hz, appears noisy or irreproducible. This, however, will have little consequence on our discussion.

Scanning ac impedance maps.—The aluminum electrode.—Figure 4 presents a contour map of the magnitude of the impedance, |Z|, of the Al electrode at 6310 Hz for the scan area presented in Fig. 2a. This figure clearly shows a radial distribution in the impedance over the aluminum electrode; the maximum impedance value occurring near the center of the electrode. A profile of this distribution *vs* |Z|, is presented in Fig. 5. The ac current distribution which corresponds to the impedance distribution, easily obtained from Ohm's law, is also presented in Fig. 5. This ac current distribution is, as expected at high frequencies, similar in contour to the well known static primary current distribution for a disk electrode in an infinitely insulating plane (22, 23).

From the contour map presented in Fig. 4 an estimation of the sensitivity of this technique can be made. The percent difference in the local ac solution current density, i_{local}, between any two adjacent points is given by

$$\text{sensitivity} = \frac{i_{local,1} - i_{local,2}}{i_{total}} \cdot 100 \qquad [3]$$

The ac current density at the electrode, i_{total}, was derived from an estimation of the average interfacial impedance from Fig. 4 and Ohm's law while the local ac solution current density for two adjacent points, $i_{local,1}$ and $i_{local,2}$, was obtained from their impedance values (Eq. [1] and [2]). In

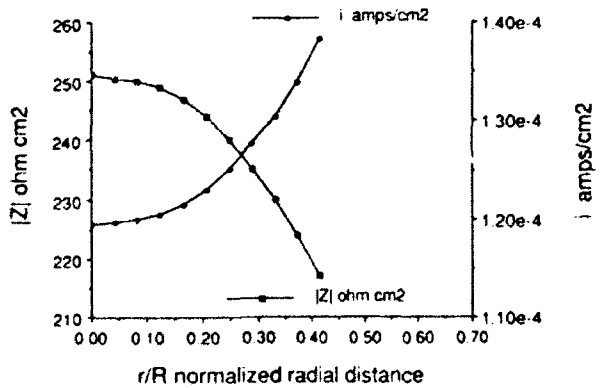

Fig. 5. The variation of the magnitude of the impedance, and the corresponding ac current density, as a function of normalized radial distance at 6310 Hz for the aluminum electrode; r—distance from the center of the electrode, R—radius of the electrode.

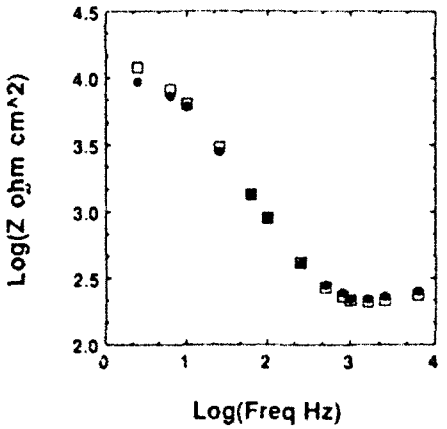

Fig. 6. Bode magnitude plots from LEIS measurements on the aluminum electrode. The (circle) is from position X-1 in Fig. 4 while the (square) is from position X-2.

this manner the sensitivity of the technique to changes in the ac solution current density is estimated from Eq. [3] to be 0.13%.

Presented in Fig. 6 are two Bode magnitude plots generated from scanning impedance measurements. These curves were made by plotting the impedance values for the two locations in Fig. 4 marked points X1 and X2 as a function of frequency. A comparison between the Bode magnitude plots for the Al electrode obtained from the scanning ac impedance technique (Fig. 6) and those obtained from traditional ac impedance techniques (Fig. 3a) is presented in Fig. 7. Using standard least squares methods (24), the impedance values from the two techniques are found to agree within 1.6 ± 1.5% over the frequency range in which scanning ac impedance maps were generated.

The aluminum/molybdenum electrode.—Representative ac impedance maps of the aluminum/molybdenum electrode at 4677 and 4.7 Hz are presented in Fig. 8 a and b, respectively, for the scan area shown in Fig. 2b. Inspection of these maps reveals that at low perturbation frequencies the impedance of the molybdenum is less than the impedance of the aluminum. At high perturbation frequencies the impedance of the electrode becomes more and more uniform as the interfacial impedance "shorts out"; i.e., the frequency of the ac current is high enough such that it may be capacitively passed across the electrode interface with virtually no impedance.

Figure 9 presents Bode magnitude plots for the aluminum and molybdenum areas of the Al/Mo electrode generated from scanning ac impedance data. Each curve in this figure illustrates the behavior of the magnitude of the im-

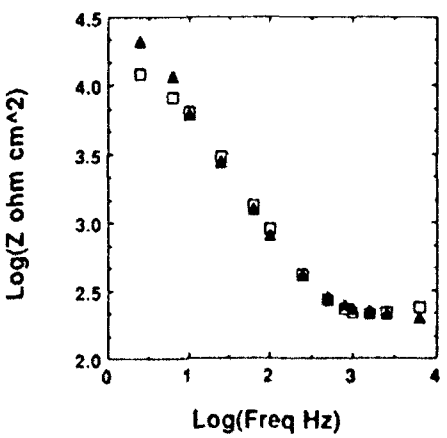

Fig. 7. A comparison of the Bode magnitude data for the aluminum electrode generated from LEIS measurements (square) and traditional EIS (triangle).

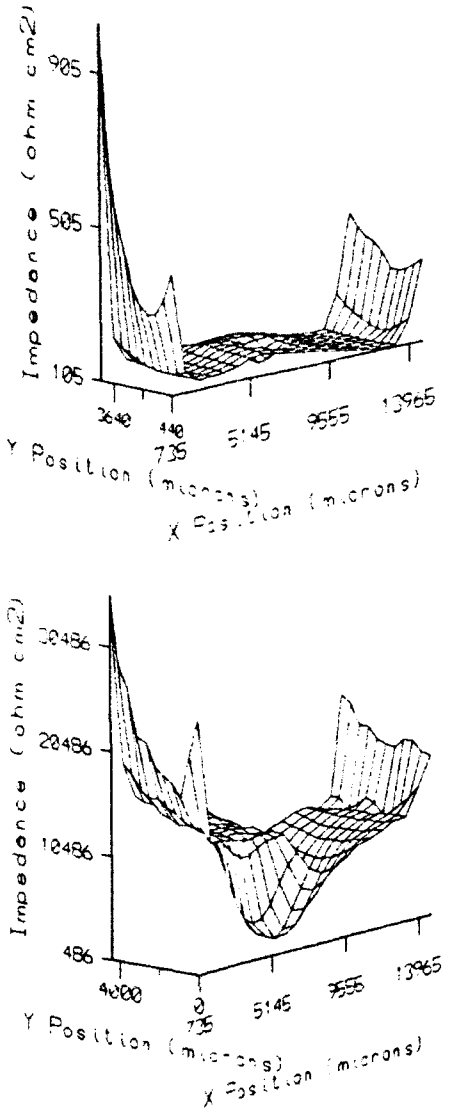

Fig. 8. 3-D maps of the magnitude of the impedance for the aluminum/molybdenum electrode generated with LEIS at a) 4677 Hz b) 4.7 Hz.

pedance for one discrete location, either over the molybdenum or aluminum portion of the Al/Mo electrode, as a function of frequency. It may be noted that in Fig. 9, in the frequency range between 100 and 6000 Hz, a dip in the Mo impedance data may be seen. This "dip" at high frequency may also be observed on close inspection of the Bode magnitude data for 99.999% Al obtained from the scanning ac impedance technique. While this anomaly is not wholly understood at this time it has had little consequence on data analysis.

A comparison between the Bode magnitude plots for the aluminum electrode obtained from traditional ac impedance techniques (Fig. 3a) and the impedance of the aluminum portion of the aluminum/molybdenum electrode obtained from the scanning ac impedance technique (Fig. 9) is presented in Fig. 10. As expected, the magnitude of the impedance of the aluminum portion of the Al/Mo electrode agrees well with the traditional ac impedance data for pure aluminum measured under the same experimental conditions. A similar comparison of scanning data from the molybdenum portion of the electrode also shows good agreement with traditional experiments except in the region of the "dip" discussed above.

Discussion

The spatial resolution of this technique is limited, in part, by the size of the probe tip; i.e., the probe will only be able to resolve (spatially) defects which are of the same size as the probe or larger. If the size of the probe is decreased to resolve smaller and smaller objects, however, the impedance of the probe will increase proportionally. This increase in probe impedance causes a corresponding decrease in the probe's ability to accurately measure the ac solution current density (19). Ideally, these two competing effects should be optimized. In this study, the size of the electrodes, Al and Mo wire, were relatively large, which allowed a probe size to be used whose impedance could be easily compensated for with readily available high impedance circuitry.

Another factor which controls the resolution of this technique is the probe/electrode separation distance. It is well known that the solution current density for these cell geometries is a function of distance from the electrode surface; i.e., the ac current tends to "spread" in solution as function of distance from the electrode (22, 23). This "spreading" effect was taken into account when the data was examined and, as a result, Bode magnitude plots were generated from LEIS data only for points on the electrode surface where the impedance data from point to point was relatively uniform or "flat". In these regions, the differential probe voltage was assumed to result from a normal ac current traveling up from the electrode through a solution volume whose cross-sectional area was defined by one grid element (the X and Y step sizes). For these areas a value for the local impedance was then derived from Eq. [2], as discussed in the background section of this paper.

The data in Fig. 7, the comparison of traditional and LEIS Bode magnitude data from the aluminum electrode, is a clear indication that this approach is valid. As discussed, the largest deviation of the LEIS data from tradi-

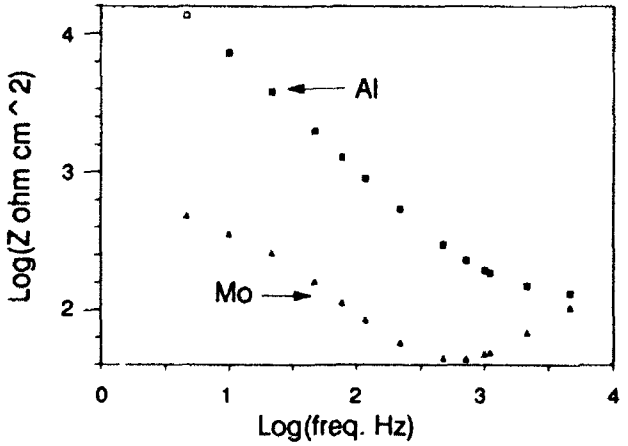

Fig. 9. Bode magnitude plots from LEIS data for the aluminum/molybdenum electrode. The (square) is from one position over the aluminum while the (triangle) is from one position over the molybdenum.

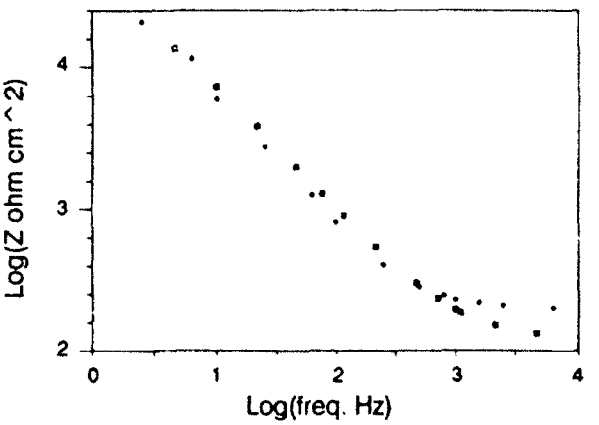

Fig. 10. A comparison of the Bode magnitude data from bulk aluminum (diamond) and one position over the aluminum portion of the Al/Mo electrode (square).

tional data in this figure is approximately 5%, which indicates that in regions where the impedance data is fairly "flat" the ac solution current density at the probe tip is a good approximation of the ac current density at the electrode. Furthermore, this argument is also supported by the data presented in Fig. 10, the comparison of Bode magnitude data obtained with traditional techniques for the Al electrode and that obtained with LEIS for the aluminum portion of the Al/Mo electrode.

As a result of this assumption, there can be an error in the local impedance measurement if the cell volume is influenced by current traveling diagonal to the electrode. Such an error is seen by closely examining Fig. 8a and b, the impedance map of the Al/Mo electrode at 4677 and 4.7 Hz, respectively. The molybdenum "defect" in the 4.7 Hz map appears to be approximately 3.0 mm in diam while in the map at 4677 Hz it appears to be approximately 1.88 mm. The true diameter of the wire is 1.27 mm. This effect is observed because not all of the ac current in the region over the aluminum near the molybdenum wire is traveling normal to the electrode. The differential probe voltage in this region is affected by both the ac current from the aluminum portion of the electrode directly below the probe traveling normal to the electrode and the normal component of the current traveling diagonally (outward) from the Mo wire. The consequence of this additional ac current from the Mo wire is that the impedance of the aluminum in the region near the Mo wire appears to be smaller than it truly is, or, conversely, the Mo defect appears larger than it truly is. The end result is that if a Bode magnitude plot for aluminum were to be generated from LEIS taken in this region near the Mo wire it would surely be in error. To obtain a true, normalized local impedance, deconvolution of the impedance maps is necessary (13). Addressing this procedure is, however, beyond the scope of this paper.

Conclusions

A LEIS system for generating local ac impedance data has been developed. In this system, as in traditional ac impedance methods, a sinusoidal voltage perturbation between the working and reference electrodes is maintained by driving an ac current between the working electrode and a distant counterelectrode. Local ac impedances are derived from the ratio of the applied ac voltage perturbation to the local ac solution current densities. The ac solution current density at any given discrete site above the electrode is obtained from potential difference measurements near the electrode surface using a probe consisting of two micro-electrodes. By measuring the ac potential difference between the micro-electrodes, and with knowledge of both the separation distance between the probe electrodes and the solution conductivity, the local ac solution current density is derived. The ac impedance properties, at each frequency of interest, of an electrode are mapped in this system, by scanning this probe across the electrode surface with high resolution X-Y translation stages.

The accuracy of the data generated with the scanning ac impedance system has been demonstrated by investigating a homogeneous 99.999% aluminum electrode system and a heterogeneous molybdenum/aluminum electrode system with LEIS, as well as, with traditional ac impedance techniques. Comparison of the Bode magnitude plot generated with LEIS for the 99.999% aluminum electrode system with the Bode magnitude plot generated with traditional techniques for the same electrode system, Fig. 8, conclusively demonstrates that the local ac impedance measurements made with this technique accurately reflect the true electrochemical properties of the electrode under investigation. Further, the ac impedance maps of the aluminum/molybdenum electrode establish that LEIS may be used to precisely locate heterogeneities in electrodes and quantify their ac impedance properties; although there was some small error in the magnitude of the impedance of the molybdenum heterogeneity between the scanning and traditional impedance techniques at high frequencies.

The application of LEIS to tactile laboratory problems, such as the investigations of the impedance properties of pits, grain boundaries, welds, and coating defects are currently in progress. These efforts include decreasing the size and configuration of the probe used to measure the local current distribution. This is being done not only to allow smaller areas on the electrode to be examined, but also to decrease the effects of shielding which increase with probe size, as shown by Tokuda (25). The results of these efforts will be presented in later publications.

Acknowledgments

The authors gratefully acknowledge the support of John Sedriks and the Office of Naval Research Grant No. N00014-89-J-1180. Hugh Isaacs is under the auspices of the U.S. Department of Energy, Division of Materials Sciences, Office of Basic Energy Sciences, Contract No. DE-AC02-76CH00016. We would also like to thank James Wagner (JHU), Doug Oursler (JHU), Robert Kelly (UVa) and Alison Davenport (BNL) for helpful discussions as well as Ken Sutter for some of the lab prep at BNL.

Manuscript submitted June 17, 1991; revised manuscript received Nov. 25, 1991. This was Paper 49 presented at the Washington, DC Meeting of the Society, May 5-10, 1991.

The Johns Hopkins University assisted in meeting the publication costs of this article.

REFERENCES

1. "Impedance Spectroscopy, J. R. Macdonald, Editor, Wiley, New York (1987).
2. I. Epelboin, C. Gabrielli, M. Keddam, and H. Takenouti, in "Electrochemical Corrosion Testing," ASTM, p. 150 (1981).
3. D. D. Macdonald and M. C. H. McKubre, *ibid.*, p. 110.
4. R. G. Kelly and P. J. Moran, *This Journal*, **134**, 31 (1987).
5. M. C. H. McKubre, Paper 480 presented at "Corrosion 87," NACE (1987).
6. M. W. Kendig and F. Mansfeld, Abstract 64, p. 105, The Electrochemical Society Extended Abstracts, Vol. 82-2, Detroit, MI, Oct. 17-21, 1982.
7. R. Oltra and M. Keddam, *Corrosion Science*, **28**, 1 (1988).
8. K. Juttner, W. J. Lorenz, M. W. Kendig, and F. Mansfeld, *This Journal*, **135**, 332 (1988).
9. J. Hitzig, K. Juttner, and W. J. Lorenz, *ibid.*, **133**, 887 (1986).
10. L. F. Jaffe and R. Nuticelli, *J. Cell Biology*, **63**, 614 (1974).
11. H. S. Isaacs, *This Journal*, **135**, 2180 (1988).
12. H. S. Isaacs, *Corrosion*, **43**, 594 (1987).
13. H. S. Isaacs, *Corrosion Science*, **28**, 547 (1988).
14. C. R. Crowe and R. G. Kasper, *This Journal*, **133**, 879 (1986).
15. H. S. Isaacs and M. W. Kendig, *Corrosion*, **36**, 269 (1980).
16. M. C. Hughes and J. M. Parks, in "Corrosion Control by Organic Coatings," NACE, p. 498 (1981).
17. J. V. Standish and H. Leiheiser, Jr., *Corrosion*, **36**, 498 (1980).
18. H. S. Isaacs and Y. Ishikawa, in "Electrochemical Techniques for Corrosion Engineering, NACE, p. 17 (1986).
19. R. S. Lillard, MSE essay, The Johns Hopkins University (1990).
20. C. Scheffey, *Rev. Sci. Instrum.*, **59**, 787 (1988).
21. E. Gileadi, E. Kirowa-Eisner, and J. Penciner, "Interfacial Electrochemistry, an Experimental Approach," Addison-Wesley, Reading, MA (1975).
22. J. S. Newman, "Electrochemical Systems," Prentice-Hall, Englewood Cliffs, NJ (1973).
23. J. Nanis and W. Kesselman, *This Journal*, **118**, 454 (1971).
24. P. R. Bevington, "Data Reduction and Error Analysis for Physical Sciences," McGraw-Hill, New York (1969).
25. K. Tokuda, T. Gueshi, K. Aoki, and H. Matusuda, *This Journal*, **132**, 2390 (1985).

IN PRESS

Faraday Discuss., 1992, 94, 000-000

94/7

Effect of Microstructure on Passive Film Formation and Breakdown of Al–Ta Alloys

J. Kruger, R. S. Lillard and C. C. Streinz
The Johns Hopkins University, Baltimore, 21218, USA

P. J. Moran
United States Naval Academy, Annapolis, MD 21402, USA

Two *in situ* techniques dynamic imaging microellipsometry (DIM) and local impedance spectroscopy (LEIS), have been applied to a study of the effect of microstructure on passive film formation and breakdown on Al-Ta alloys. DIM acquires ellipsometric data (thickness and optical constants of the films on surfaces) at a spatial resolution of *ca.* 20 μm using a radiometric full-field imaging approach. LEIS is an electrochemical impedance technique that generates local a.c. impedance data by measuring a.c. solution current densities very near the microstructural features of an electrode surface. The DIM technique was used to look at passive film formation at (*a*) the Al_3Ta precipitate, (*b*) the dealloyed zone adjacent to the precipitate and (*c*) the solid solution phase that is present in Al-Ta alloys. The DIM technique observed different film thicknesses and optical constants for the films that form on these phases at potentials in the passive regions. The LEIS technique was used to study the precipitate and the region surrounding it under conditions where passive film breakdown occurs. Using these techniques, insight was obtained into the passive film formation and breakdown processes that control localized corrosion

This paper describes two *in situ* techniques, dynamic imaging microellipsometry (DIM)[1-3] and local electrochemical impedance spectroscopy (LEIS),[4] that we have applied to a study of the effect of microstructure (grains, grain boundaries, precipitates *etc.*) on passive film formation and breakdown.

While these techniques do not have the resolution of some of the other techniques included in this Faraday Discussion of high-resolution techniques for studying the solid/liquid interface such as STM, they can greatly contribute to a better understanding of how microstructure effects passive film formation and breakdown, two of the major aspects affecting corrosion processes. These techniques can measure the formation and breakdown rates (thickness *vs.* time) and film properties (optical constants, impedance and capacitance) of passive films on microstructural features. Such measurements show promise of increasing our understanding of the influence of thin films on important processes occurring at the liquid/solid interface.

In order to show the capabilities of DIM and LEIS, we will describe their application in this study to the role played by the Al_3Ta precipitates that form in Al-Ta alloys in affecting susceptibility to pitting, a phenomenon that depends strongly on the tendency of passive films to form and breakdown. It has been found that when Ta is added to Al, sputter-deposited films of these alloys exhibit significantly higher critical pitting potentials (a measure of pitting tendency) than the more susceptible pure Al.[5,6]

Dynamic Imaging Microellipsometry

Ellipsometry is an optical technique that enables the thickness and complex refractive index of thin films on metal surfaces to be measured *in situ*.[7] Since many corrosion and electrochemical processes involve film formation and breakdown, ellipsometry has proven to be a valuable research tool for studying corrosion.[8] Traditional ellipsometry, however, is by nature a surface-averaging technique and is limited in its ability to study localized corrosion processes such as the effects of microstructure on passive film growth and breakdown.

Cohn *et al.*[1-3] developed DIM in order to overcome the above limitation. In contrast to other techniques aimed at acquiring ellipsometric data with high spatial resolution,[9,10] DIM is a radiometric full-field imaging approach to ellipsometry. Good spatial resolution (*ca.* 20 μm) and precision in addition to good temporal resolution (minutes) were demonstrated. The DIM approach utilized the standard polarizer, specimen, compensator, analyser (PSCA) ellipsometry configuration in combination with an imaging lens, a charged coupled device (CCD) video camera and digital image processing techniques to acquire high spatial resolution ellipsometric data with good temporal resolution. DIM produces digitized grey scale maps (called ellipsograms) of the ellipsometric parameters Δ (change in phase) and ψ (change in relative amplitude) that enable the determination of film thickness with a resolution of *ca.* 0.1 nm and film and substrate refractive indices. The ellipsograms are produced by acquiring four digitized intensity maps each at a distinct polarizer setting and then calculating the Δ and ψ maps point by point using the appropriate algorithms.

Recent work[11] describes the development of a third-generation DIM system and its application to the *in situ* study of passivation. Ellipsogram-to-ellipsogram temporal resolution for this system is *ca.* 20 s. A sample *in situ* ellipsogram of a passivated iron surface is illustrated in Fig. 1. Note that the grey levels observed are linearly proportional to Δ and ψ. The grain structure is 'observed' in the Δ map but not in the ψ map, indicating differences in the passive film thickness over the respective grains.

A.c. impedance, which is also known as electrochemical impedance spectroscopy (EIS), is a powerful non-destructive *in situ* technique which has been used extensively to

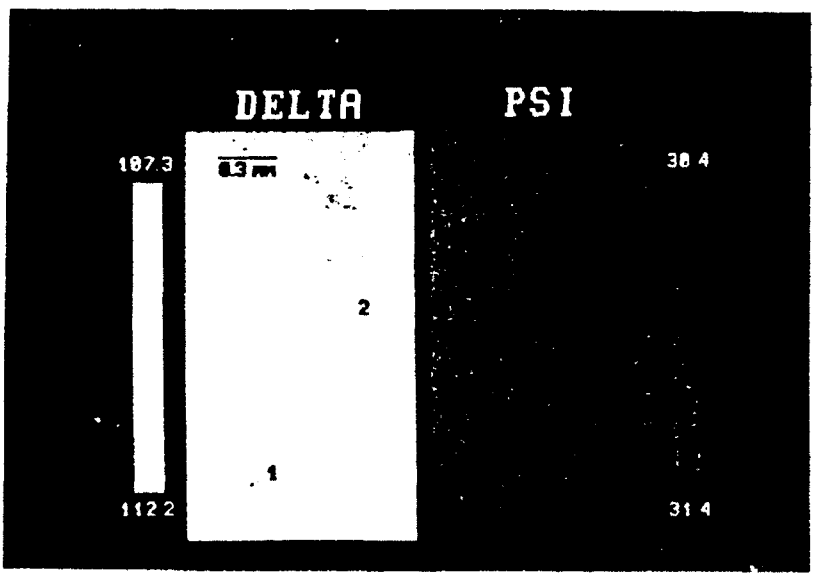

Fig. 1 Ellipsogram for iron after 5 h polarization at 500 mV *vs.* SCE in a borate buffer solution. Note that the grains can be 'observed' in the Δ map but not in the ψ map, indicating passive film thickness differences from grain to grain. (From ref. 7)

investigate electrochemical systems.[12] EIS applies a small sinusoidal voltage perturbation across the electrochemical interface. Impedance data for the whole electrode are then generated by measuring the ratio of the voltage perturbation and its current response as a function of frequency, ω. The impedance data generated are most commonly presented in either Nyquist format ($-Z_{imaginary}$ *vs.* Z_{real}) or as Bode plots [$|Z|$ *vs.* ω and θ (phase angle) *vs.* ω].

Because the current response of the whole electrode is used to generate impedance data, a surface averaged measurement results, which can lead to difficulties if one is interested in determining the effects of microstructural features on local phenomena such as localized corrosion processes. The lack of uniformity arises because the frequency dependence of the current distribution in the vicinity of a corrosion site is markedly different from that near an inactive or passive area. EIS has been applied to localized corrosion systems, but data analysis for these systems is complex.[13,14] For this reason, a technique (LEIS) for generating local a.c. impedance data has been developed[4] to investigate localized corrosion due to multiphases, grain-boundary effects or other surface heterogeneities which may occur on an electrode surface.

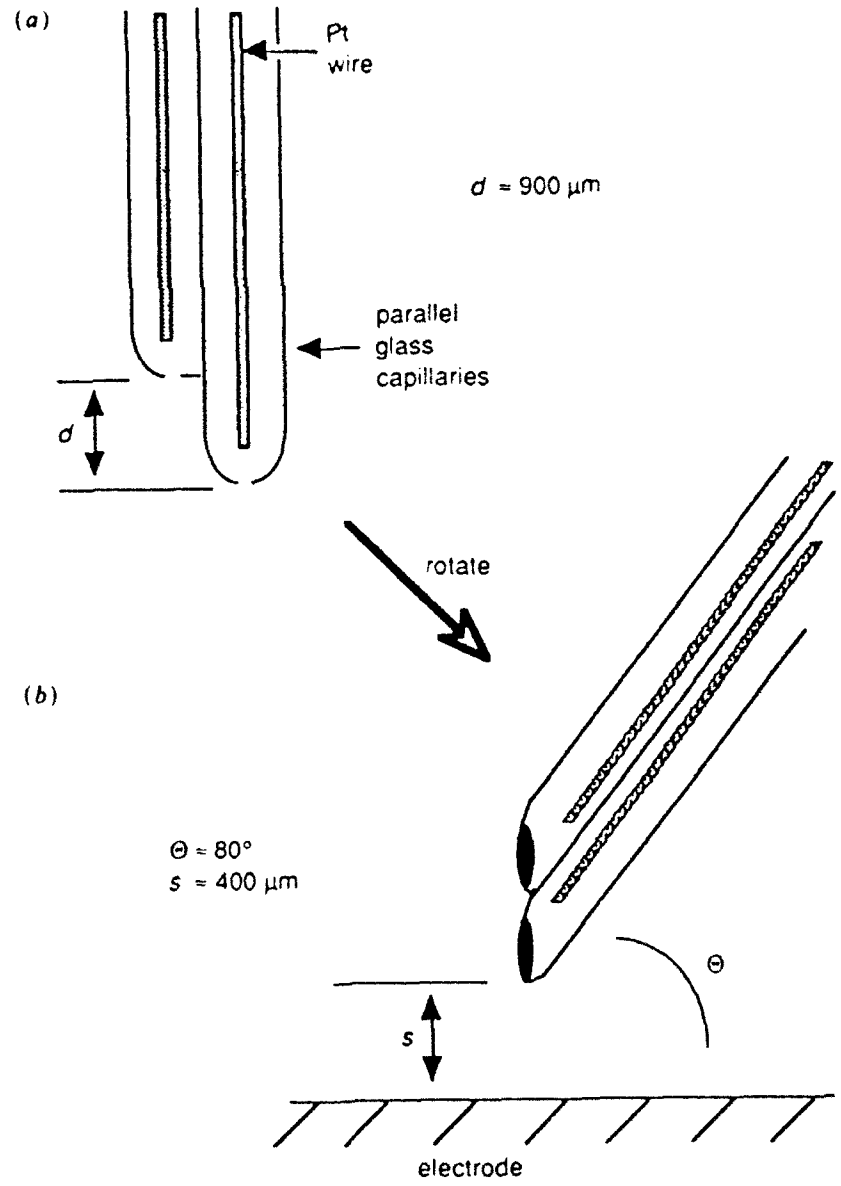

Fig. 2 The two-electrode probe used to make local a.c. impedance measurements. (From ref. 4)

The basis for this technique depends on the premise that the a.c. solution current densities very near the working electrode, in a conventional three-electrode a.c. impedance measurement, are proportional to the local impedance properties of the electrode.

Other investigators have demonstrated that the current distribution very near an electrode may be mapped in three dimensions; each, or any combination, may be mapped for an electrode surface by choosing the correct probe geometry.[15,16] To simplify data analysis, this technique measures only the component of the a.c. current normal to the electrode. Because current and potential lines are perpendicular, it is necessary to measure the a.c. potential drop between planes parallel to the electrode to measure the a.c. solution current density normal to the electrode. An effective map of local impedance

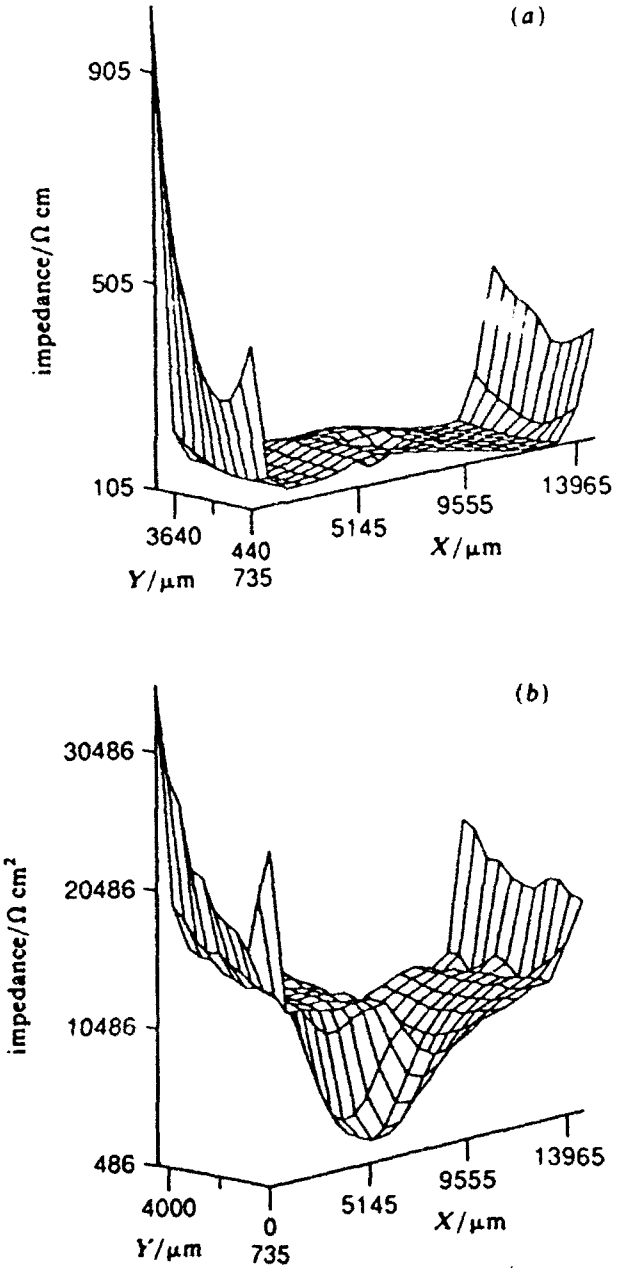

Fig. 3 3D maps of the magnitude of the impedance for the aluminium/molybdenum electrode generated with LEIS at: (*a*) 4677 Hz, (*b*) 4.7 Hz. (From ref. 4)

properties of an electrode requires that this a.c. potential drop measurement must be made on a relatively small scale. To accomplish this, the two-electrode microprobe, shown in Fig. 2, was designed.

An example of the three-dimensional maps generated by LEIS is given in Fig. 3. It shows the variation in impedance in the $X-Y$ plane of the surface of a model electrode that contains a 0.127 cm diameter wire of Mo force moulded in the centre of an Al cylinder.

Application of DIM and LEIS to a Study of the Effect of Microstructure on Passive Film Formation and Breakdown on an Al Alloy

To explore the capability of DIM and LEIS to examine *in situ* passive film formation and breakdown processes at a resolution level of the microstructures existing in an Al-Ta alloy, it was necessary to prepare an alloy that contained Al_3Ta precipitates whose size was within the detectability of the two techniques; 20 μm for DIM and 300 μm for LEIS. An Al-1.5 atom % Ta alloy was prepared and heat treated in a manner to produce large (*ca.* 50 μm) Al_3Ta precipitates surrounded by essentially pure Al (the equilibrium concentration of Ta in Al is *ca.* 0.02 atom % Ta.[17]). The specimens provided two of the microstructural features existing in Al-Ta alloys that are relevant to the study of localized passive film formation and breakdown, Al_3Ta surfaces and the dealloyed region adjacent to the A_3Ta precipitates. To examine the areas where no dealloying occurred, sputter-deposited Al-Ta films were also examined by DIM.

DIM Studies

Fig. 4(*a*) shows an ellipsogram of a surface of Al-1.5 atom % Ta containing Al_3Ta precipitates at the free-corrosion potential ($E_{corr} = -750$ mV *vs.* SCE) in a pH 7.2 buffered borate-boric acid ($Na_2B_2O_7$-HBO_3) solution. The bright regions in the Δ maps and corresponding dark regions in the ψ maps are the Al_3Ta precipitates. The micron marker in the figure shows that these precipitates are *ca.* 30-50 microns in diameter. This ellipsogram demonstrates that the intial Δ value of the precipitate is higher than the Al matrix and the initial ψ value is lower than the Al matrix. The ellipsogram in Fig. 4(*a*) allows the optical constants of the Al_3Ta precipitate and the Al matrix to be measured as a necessary first step towards determining the film thickness amd optical constants of the passive film that forms at higher potentials.

Fig. 4(*b*) is an ellipsogram of the same region polarized at an applied potential of 0 V *vs.* SCE for 15 min. Obtaining ellipsograms at different times [ellipsogram in Fig. 4(*a*) being at zero time) at a potential in the passive region of the anodic polarization curve enables the determination of the rate of passive film formation for each of the microstructural features. Comparison of the Δ map in ellipsogram 4(*b*) to the Δ map in ellipsogram 4(*a*) shows a decrease in contrast between the precipitates and matrix. This shows that the Δ values for the precipitate have decreased more than that of the matrix upon polarization, indicating growth of a thicker film. Extraction of Δ and ψ values from the ellipsograms demonstrates this further. Fig. 5 plots the change in film thickness *vs.* time for applied potentials of 0.0 and 2.0 V *vs.* SCE. Note that at 0.0 V *vs.* SCE the change in thickness of the passive film on the precipitate is approximately twice that of the matrix (1.0 to 0.5 nm). At 2.0 V *vs.* SCE, however, the change in passive film thickness over the matrix is greater than that over the precipitate (2.9 to 2.5 nm). The average indicies of refraction of the films formed on the Al matrix and Al_3Ta were 1.60 and 1.78 + 0.055i, respectively. Examination of film formation on sputtered Al-25 atom % Ta and Al-8 atom % Ta found film thicknesses less than those measured for the matrix or the Al_3Ta precipitate.

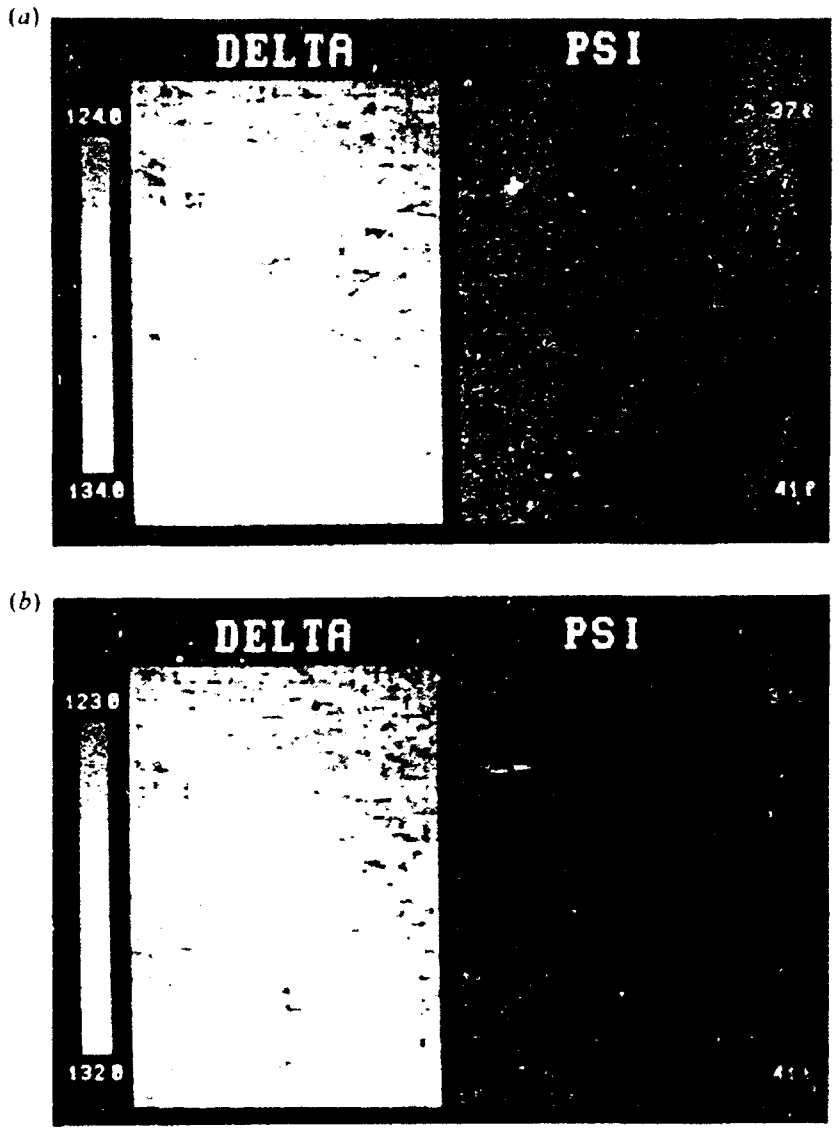

Fig. 4 Ellipsograms for the Al_3Ta-Al matrix system. The bright regions in the Δ maps and the dark region in the ψ maps are the Al_3Ta precipitates. Recall that the grey levels are proportional to Δ and ψ: (*a*) obtained at $E_{corr} = -750$ mV *vs.* SCE, (*b*) obtained after passivation at 0 V *vs.* SCE for 15 min.

These passive film thickness results are surprising. It was expected that the precipitates would form thinner films at all applied potentials owing to enrichment of highly protective Ta_2O_5 in the passive layer. Thinner films over the precipitate are observed at higher potentials (2.0 V *vs.* SCE) but not at low potentials (0.0 V *vs.* SCE). At present this is not understood. The index of refraction of the film over the matrix is consistent with that formed on pure aluminum.[18] The real portion of the index of the film over the precipitate is consistent with a film containing both Al_2O_3 and Ta_2O_5. Muth[19] showed that the index of Ta_2O_5 is 2.22 and that an Al-Ta alloy forms a film whose index is between that of Al_2O_3 and Ta_2O_5 depending on the alloy composition. A first approximation using the law of mixtures indicates that Al_3Ta would be expected to form a film with an index of 1.75. Note also that the film over the Al_3Ta is observed to have a small absorption coefficient. The physical basis for this is not presently understood since the index of the passive layers on Al and Ta are entirely real. A small absorption coefficient indicates that the passive film probably has a limited electrical conductivity (unlike

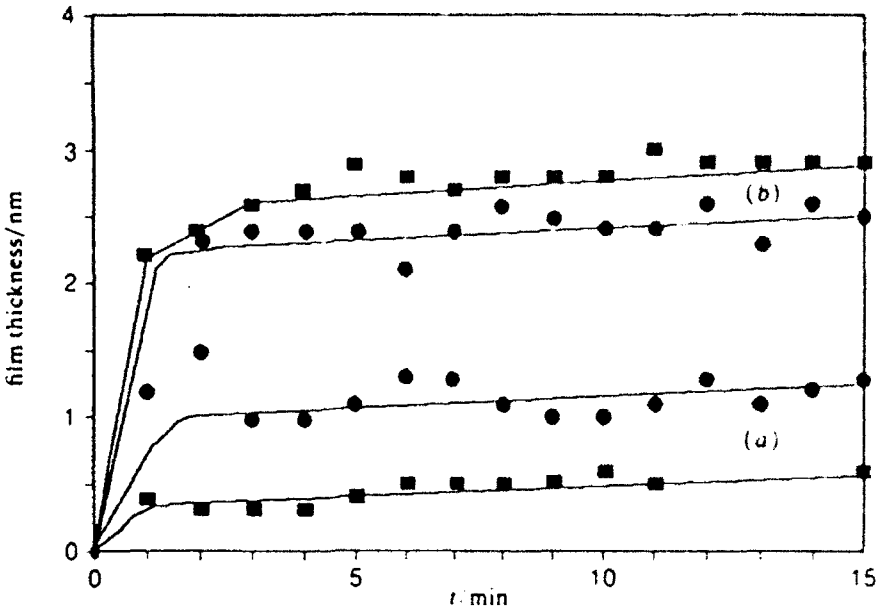

Fig. 5 Film thickness *vs.* time for the Al_3Ta precipitate (●) and Al matrix (■) when polarized at 0 (*a*) and 2 V *vs.* SCE (*b*). Note that at 0 V the passive film on the precipitate is thicker than on the matrix. The opposite is true at 2 V

Al_2O_3 and Ta_2O_5 which are insulators). This is consistent with the observation in this study and another[11] that at high overpotentials (several volts) oxygen is evolved at the precipitates.

LEIS Studies

LEIS measurements were conducted on the Al 1.5 atom % Ta alloy depicted in Fig. 6. The precipitates, Al_3Ta, in this sample were of the order of 10–100 μm in diameter, although one large precipitate measuring *ca.* 1 mm in diameter was found. The segregation of the precipitates to one side of the sample as shown in Fig. 6, was due to gravity.

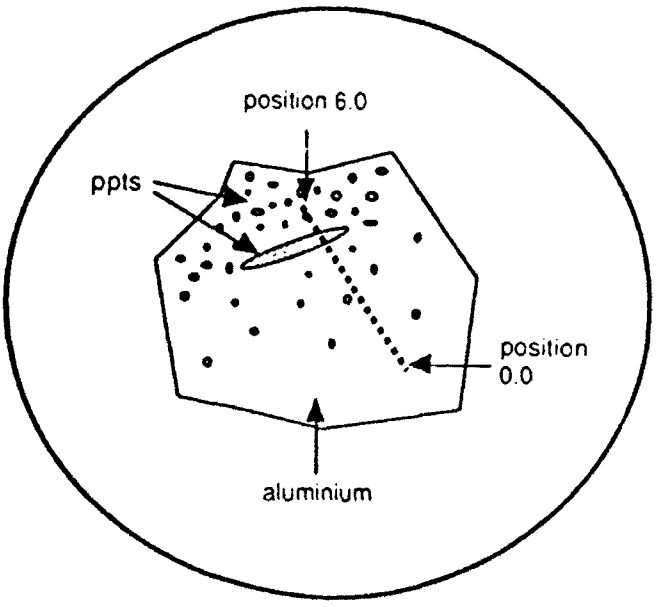

Fig. 6 The Al-1.5 % Ta alloy used for the LEIS experiments

This sample was studied in an aerated 0.1 mol dm^{-3} sodium chloride solution buffered to pH 7.2 with 0.5 mol dm^{-3} boric acid-0.05 sodium borate and held at E_{corr}, −750 mV *vs.* SCE. LEIS line scans of this sample were generated by stepping the probe in increments of 250 μm from the precipitate-depleted region to the precipitate-rich region (see Fig. 6) and were conducted over the frequency range 1-10 000 Hz.

Two LEIS line scans at 2.4 and 2400 Hz, which plot the magnitude of the impedance as a function of position, are presented in Fig. 7. As shown in these figures, position 0.0 is in a region of the sample which is mostly Al, the large precipitate is centred at about the 4.5 position and, position 6.0 is in a region of high precipitate density. Notice in these figures that regions of high precipitate concentration have low impedance values. The dip in the high-frequency impedance data, between 100 and 10 000 Hz, results from changes in the current density distribution and is discussed elsewhere.[4] The lowest

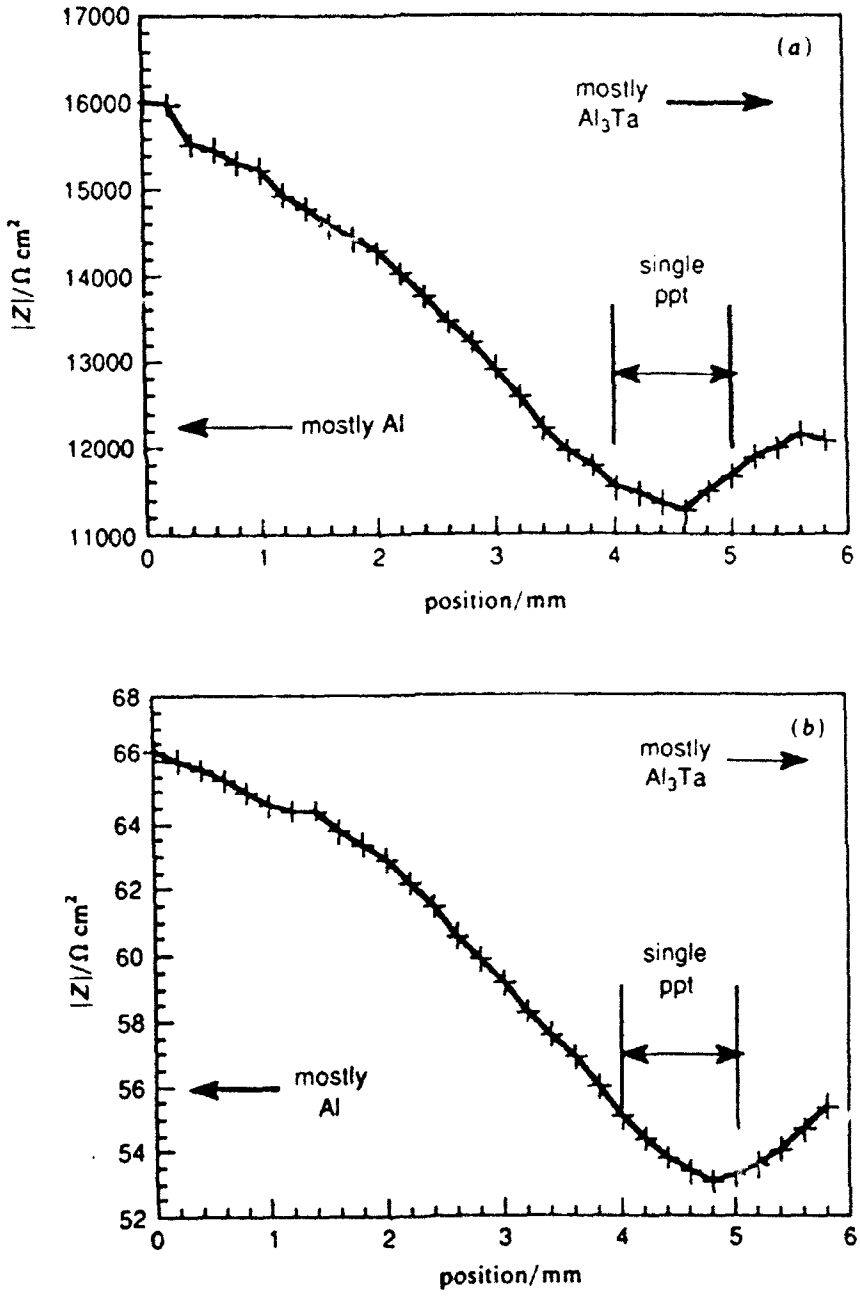

Fig. 7 LEIS line scans of the sample depicted in Fig. 6: (*a*) at 2.4 Hz and (*b*) at 2400 Hz

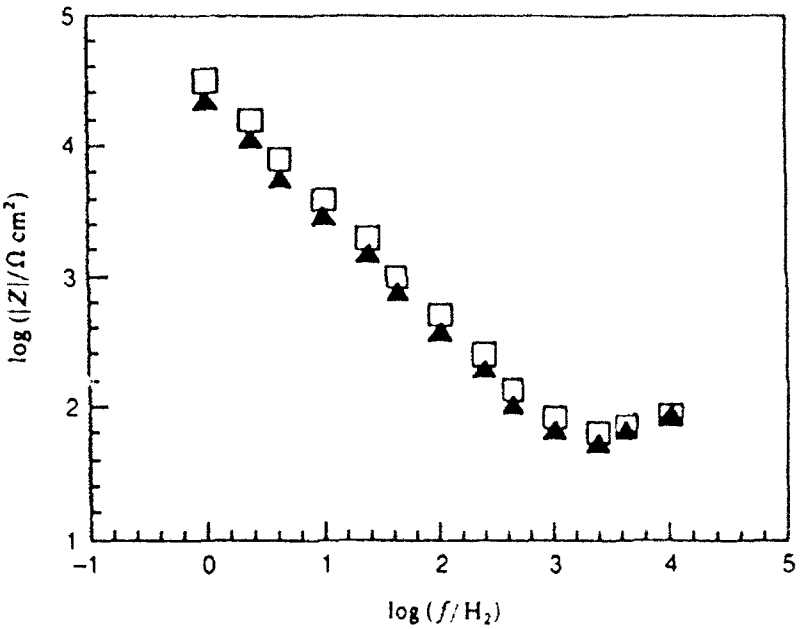

Fig. 8 Bode magnitude plot generated from LEIS data for the Al_3Ta precipitate (▲) and the Al matrix (□)

impedance in these line scans is that of the large precipitate, which is *ca.* 500 Ω cm² lower than the impedance of the aluminium portion of the sample at 2.4 Hz. This point is re-emphasized in Fig. 8, a Bode magnitude plot generated from LEIS by plotting the log of the magnitude of the impedance from one position, either over the Al or the Al_3Ta precipitate, as a function of frequency. While LEIS data were not generated at frequencies low enough to enable a charge-transfer impedance for the precipitate and Al to be resolved, it is clear from Fig. 8 that the capacitance of the film over the precipitate is slightly larger than the capacitance of the film over the Al. This indicates that the two films differ somewhat in composition and/or thickness.

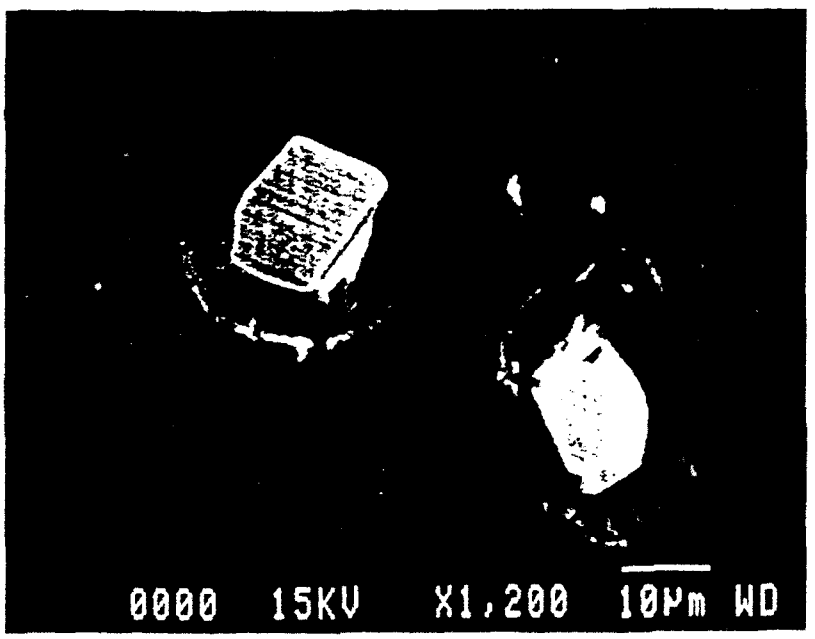

Fig. 9 SEM photograph of the preferential dissolution of Al around an Al_3Ta precipitate after 48 h immersion in 0.1 mol dm^{-3} NaCl

The above LEIS measurements and our DIM measurements have shown that the precipitate film and the dealloyed region film differ in thickness as well as composition and/or structure. Therefore, it is likely that there is an incoherent interface between the two films that is susceptible to localized attack.[20] Local strains or flaws such as dislocations at the interface may promote the Cl^- adsorption or ingress that leads to breakdown. This hypothesis is supported by Fig. 9, an SEM photograph of two of the precipitates in this alloy after immersion in 0.1 mol dm^{-3} NaCl at E_{corr} for 48 h. This micrograph clearly shows the preferential dissolution of Al around a Al_3Ta precipitate. It is apparent that the interface between the two films serves as a site for local attack, although a cathodic precipitate may provide the driving force for propagation.[21]

Concluding Remarks

The role played by microstructural features on the passivation and breakdown processes that lead to localized corrosion have been examined for presumably the first time by the new techniques of DIM and LEIS. An examination of the passivation of an Al-Ta alloy found, contrary to expectations, that the Al_3Ta precipitate formed a thicker film than the film on the solid solution region that surrounds the dealloyed region exhibited the smallest thickness. The optical constant of the Al_3Ta film had an absorption coefficient that indicated some electronic conductivity, which explains an earlier observation that oxygen can be evolved on the precipitate's surface. The LEIS study of microstructural effects under breakdown conditions found that the film on the Al_3Ta had a higher capacitance than the dealloyed region surrounding the precipitate, indicating that the precipitate film has different properties from the dealloyed region. This difference in film properties may be responsible for the breakdown that leads to the localized attack observed in Fig. 9.

This research was supported by the Office of Naval Research Contract no. N00014-89-J-1180. The authors are grateful to Dr. John Sedriks for his role in providing this support. C.C.S. was supported throughout this work by a National Science Foundation Award. We also thank Frank Biancaniello of the National Institute of Standards and Technology who produced, using great ingenuity, the specimens used in this study.

Reference

1 R. F. Cohn, J. W. Wagner and J. Kruger, *J. Electrochem. Soc.*, 1988, **246**, 1033.
2 R. F. Cohn, J. W. Wagner and J. Kruger, *Appl. Opt.*, 1988, **27**, 4664.
3 R. F. Cohn and J. W. Wagner, *Appl. Opt.*, 1989, **28**, 3187.
4 R. S. Lillard, P. J. Moran and H. S. Isaacs, *J. Electrochem. Soc.*, 1992, **139**, 1007.
5 G. S. Frankel, M. A. Ruissak, C. V. Johnes, Mi Mirzamaani and V. A. Brusic, *J. Electrochem. Soc.*, 1989, **136**, 1243.
6 G. D. Davis, W. C. Moshier, T. L. Fritz and G. O. Cote, *J. Electrochem. Soc.*, 1990, **137**, 422.
7 R. M. A. Azzam and N. M. Bashara, *Ellipsometry and Polarized Light*, Elsevier, New York, 1987.
8 J. Kruger, *J. Phys. (Paris) Colloq.* 1977, **38**, C5, 129.
9 K. Sugimoto and S. Matsuda, *J. Electrochem. Soc.*, 1983, **130**, 2323.
10 A. J. Hurd and C. J. Brinker, *J. Phys. (Paris)*, 1988, **49**, 1017.
11 C. C. Streinz, J. W. Wagner, J. Kruger and P. J. Moran, *J. Electrochem. Soc.*, 1992, **139**, 711.
12 *Impedance Spectroscopy*, ed. J. R. Macdonald, Wiley, New York, 1987
13 R. Oltra and M. Keddam, *Corrosion Sci.*, 1988, **28**, 1.
14 K. Juttner, W. J. Lorenz, M. W. Kendig and F. Mansfeld, *J. Electrochem. Soc.*, 1988, **135**, 332.
15 H. S. Isaacs and Y. Ishikawa, in *Electrochemical Techniques for Corrosion Engineering*, ed. R. Baboian, NACE, Houston, TX, 1986, pp. 17-000.
16 C. Scheffey, *Rev. Sci. Instrum.*, 1988, **50**, 787.
17 *Metals Handbook, Metallography, Structures and Phase Diagrams*, Am. Soc. Metals, Metals Park, OH, 8th edn., 1973, vol. 8, p. 264.
18 L. Young, *Anodic Oxide Films*, Academic Press, New York, 1961, p. 216.
19 D. G. Muth, *J. Vac. Sci. Technol.*, 1969, **6**, 749.

20 M. Metzger and J. Zahavi, in *Passivity of Metals*, ed. R. P. Frankenthal and J. Kruger, Electrochemical Soc., Princeton, NJ, 1978, pp. 960-972.
21 J. R. Scully, R. P. Frankenthal, K. J. Hanson, P. J. Siconoldii and J. D. Sinclair, *J. Electrochem. Soc.*, 1990, 137. 1365.

Paper 2/02732A; *Received* 26*th May*, 1992